Computational simulation of the fluid flow in a subsonic jet-pump

Manuel Orlando Sandoval Pinto

Trabajo de grado presentado para optar al título de Ingeniero Aeroespacial

Asesor
Diego Francisco Hidalgo López, Doctor (PhD) en Dinámica de Fluidos Computacional

Universidad de Antioquia
Facultad de Ingeniería
Ingeniería Aeroespacial
El Carmen de Viboral, Antioquia, Colombia
2024

Cita	Sandoval Pinto [1]
Referencia Estilo IEEE (2020)	[1] M. O. Sandoval Pinto, “Computational simulation of the fluid flow in a subsonic jet-pump”, Trabajo de grado profesional, Ingeniería Aeroespacial, Universidad de Antioquia, El Carmen de Viboral, Antioquia, Colombia, 2024.

Dedicatory

I dedicate this degree work to my family, whose constant support has been the basis of my academic journey.

To my beloved Mariana Toro Ramirez, my tireless partner throughout this university journey and life. Your presence has been my beacon in moments of doubt and confusion, and your unwavering faith in my ability has been my engine to reach new heights. With your endless motivation, you have awakened in me a renewed determination and a deeper sense of purpose. Your constant inspiration has illuminated my path and shaped my personal growth in ways I never thought possible.

To my dear father Jairo Sandoval Sanchez, whose love and teachings have shaped my perspective towards study and core values from an early age. Your unceasing commitment to my education has been the cornerstone of my development, guiding me towards understanding the importance of contributing to the progress of society in a conscious and committed manner.

To my adored mother Maria Lucía Pinto Lara, your constant care and support provided the foundation of my integral formation. Your unflinching dedication and encouragement have been my inspiration to pursue my goals and follow my dreams. Your unconditional love has been the shining light that illuminates my path, guiding me through every challenge and celebrating with me every accomplishment.

To my sister Ana María Sandoval Pinto, my trusted supporter and accomplice at every stage of my life. Your presence has filled my days with laughter, complicity and an indelible connection that has enriched my being. Your constant encouragement and unconditional support have been a source of inspiration and strength, reminding me of the importance of perseverance and gratitude in the pursuit of our purposes. Your resilient spirit and love have left an indelible mark on my path to personal and academic growth.

Acknowledgments

In the culmination of this transformative educational odyssey, I find myself indebted to countless individuals whose tireless efforts have intricately shaped my academic journey. With heartfelt gratitude, I extend my deepest appreciation to those who have consistently provided unwavering support, invaluable guidance, and endless inspiration. Their insightful contributions have not only facilitated my academic pursuits but have also left an indelible imprint on my personal and professional growth.

I am immensely grateful to Ph.D. Diego Francisco Hidalgo López for his dedication, profound guidance, and scholarly expertise, which have been instrumental in the culmination of this work. His commitment to academic excellence and constructive criticism has not only elevated the quality of this research but has also significantly influenced my intellectual expansion and research capabilities. His mentorship has kindled a relentless curiosity within me, driving me to explore new frontiers in this intricate field.

My heartfelt gratitude extends to Ph.D. Sébastien Poncet for his pivotal role in the genesis and conceptualization of this project. I feel deeply honored and grateful for the warm inclusion in this endeavor, and for the collective efforts and unwavering support of the entire team at the Laboratoire de Mécanique des Fluides, Thermique et Energétique de l'Université de Sherbrooke. Their collaborative spirit, benevolence, collective wisdom, and relentless dedication have profoundly enriched my understanding and contributions to this project. I remain sincerely appreciative of the opportunity to collaborate with such an inspiring and devoted group.

I am especially thankful for the significant mentoring and collaboration with Ph.D. candidate Akbar Ravan Ghalati for this work. His expert guidance, persistent support, and insightful supervision have played an indispensable role in shaping the trajectory and excellence of this project and my passion for this field. His dedication and profound contributions have deeply enriched my learning experience and have played a crucial role in the accomplishment of this work. And of whom I value his quality as a human being and the way in which this is reflected in the work he does, demonstrating excellence in every aspect.

Furthermore, my appreciation extends to the Mitacs Globalink Research Internship program, and its dedicated team members and facilitators, for providing the essential framework and financial support that contributed to the successful completion of this work during my internship at the University of Sherbrooke.

TABLE OF CONTENTS

LIST OF TABLES

LIST OF FIGURES

STANDS, ACRONYMS, AND ABBREVIATIONS

Acronyms and abbreviations:

CFD	Computational Fluid Dyamics
DNS	Direct Numerical Simulation
EVM	Eddy Viscosity Models
Fig.	Figure
IEEE	Institute of Electrical and Electronics Engineers
LES	Large Eddy Simulation
N-S	Navier-Stokes
PhD	Philosophiae Doctor
RANS	Reynolds-Averaged Navier-Stokes
TDR	Turbulence Dissipation Rate
TKE	Turbulence Kinetic Energy
nxp	Nozzle-tip spacing to the beginning of the throat

Symbols and units:

C_p	Pressure coefficient
η	Efficiency
FR	Flow ratio
PR	Pressure ratio
$\dot{m}$	Mass flow rate
Q	Volumetric flow rate
P / p	Pressure
A_r	Area ratio
V	Velocity
γ	Specific weight
g	Gravitational acceleration
ρ	Density
K	Loss coefficient
D	Diameter

u/v/w	Flow / velocity in the x/y/z direction
U/V/W	Mean flow in the x/y/z direction
δ	Kronecker Delta
μ	Viscosity
$\bar{S}$	Mean rate of strain tensor
ν_t	Eddy viscosity
k	Turbulence kinetic energy
ε	Turbulence kinetic energy dissipation rate
ω	Specific turbulence kinetic energy dissipation rate
y	Vertical distance to the wall
u_τ	Friction velocity
ν_k	Kinematic viscosity
τ_w	Wall shear stress
N	Newtons
M	Meters
Re	Reynolds number
t / T	Time

Subscripts and superscripts:

1	Primary
2	Secondary
out	Output
x	Linear positions measured from throat beginning
n	Nozzle or at the nozzle-tip
t	Throat
d	Diffuser
p	Primary inlet
s	Secondary inlet
'	Mixing flow / fluctuations
' '	Fully mixed flow
–	Averaged over time

RESUMEN

Este estudio busca desarrollar los elementos computacionales necesarios para predecir mediante simulaciones CFD, el desempeño de una bomba-jet subsónica operando con agua, centrándose en la relación de presiones, relación de flujo, eficiencia energética y el campo de flujo interno. Los modelos RANS de turbulencia *k-ω SST* y *k-ε*, con funciones estándar, escalable y tratamiento mejorado de pared, se utilizan para simular el comportamiento bajo ocho relaciones de flujo diferentes, para tres espaciamientos de boquilla distintos. Estas geometrías, discretizadas mediante mallas bien estructuradas, se revisan en términos de calidad e independencia de malla mediante un análisis de sensibilidad y comparación con la capa límite teórica. Los resultados se comparan entre sí y con datos experimentales disponibles en la literatura para validar el entorno de simulación implementado y determinar que modelos capturan mejor cada aspecto del desempeño. El análisis numérico muestra que las simulaciones predicen adecuadamente los fenómenos que rigen las bombas-jet, donde el error relativo promedio en eficiencia de *k-ε* es del 7.3% y para *k-ω SST* 8.47%, análogamente, para el coeficiente de presión que da cuenta del bombeo del dispositivo es del 10.68% y 3.21% respectivamente. Adicionalmente, los contornos de velocidad y presión comprueban que a menor relación de flujo se da una mayor relación de presiones entre la salida y las entradas, y a medida que la zona de mezcla se acerca al final de la garganta sin sobrepasarla, producto de un incremento en la relación de flujo, la eficiencia alcanza su máximo, como se observa en investigaciones previas.

Palabras clave — **Modelos RANS, CFD, bomba-jet, eficiencia, flujo interno.**

ABSTRACT

This study aims to develop the computational elements necessary to predict through CFD simulations, the performance of a subsonic jet pump operating with water, focusing on the pressure ratio, flow ratio, energetic efficiency, and the internal flow field. The RANS-based turbulence models *k-ω SST* and *k-ε*, along with standard, scalable, and enhanced wall functions are used to simulate the behavior under eight different flow ratios for three different nozzle spacings. These geometries, discretized using well-structured meshes, are reviewed in terms of mesh quality and mesh independence through a sensitivity analysis and the comparison with the theoretical boundary layer. The results are compared with each other and with experimental data available in the literature to validate the implemented simulation environment and determine which models best captures each aspect of the performance. Numerical analysis shows that the simulations accurately predict the phenomena governing the jet-pumps, where the average relative error in efficiency for *k-ε* is 7.3% and for *k-ω SST* is 8.47%, analogously, for the pressure coefficient that accounts for the device pumping it is 10.68% and 3.21% respectively. Additionally, the velocity and pressure contours prove that at lower flow ratios there is a higher pressure ratio between the outlet and the inlets, and as the mixing zone approaches the end of the throat without exceeding it, as a result of an increased flow ratio, the efficiency reaches its maximum, as observed in previous research.

Keywords — **RANS modeling, CFD, jet-pump, efficiency, internal flow.**

I. INTRODUCTION

A. Jet-pumps devices

Jet-pumps are devices that essentially operate by suctioning a secondary fluid through the action of a low-pressure zone, created by a primary fluid at high velocity, and mixing both fluids through geometrical changes and turbulent phenomena, allowing them to transport fluids safely and efficiently or increase the mass flow of a process. Moreover, since these types of devices have no moving parts, they are a simple, robust, cost-effective, and efficient alternative. For this reason, they have been used as pumping tools in industries such as the oil industry, transport mechanisms of hazardous substances in the chemical industry, jet cooling systems, desalination devices or mixing of substances, among other applications where there is no nearby power supply, maintenance conditions are complicated, or the criticality of the system requires it [1], [2].

In a traditional subsonic jet-pump as the one shown in Fig. 1, composed from [3], [4], it is possible to distinguish four main sections, the converging primary fluid nozzle, the secondary fluid chamber, the mixing throat, and the diverging diffuser. Each of these sections fulfills a specific function within the internal behavior of the fluids and, therefore, it has characteristics that modify the properties of the fluid throughout the system, hence, it is natural to intuit that there is a great variety of combinations of geometries, design and operational characteristics that better satisfy different use cases.

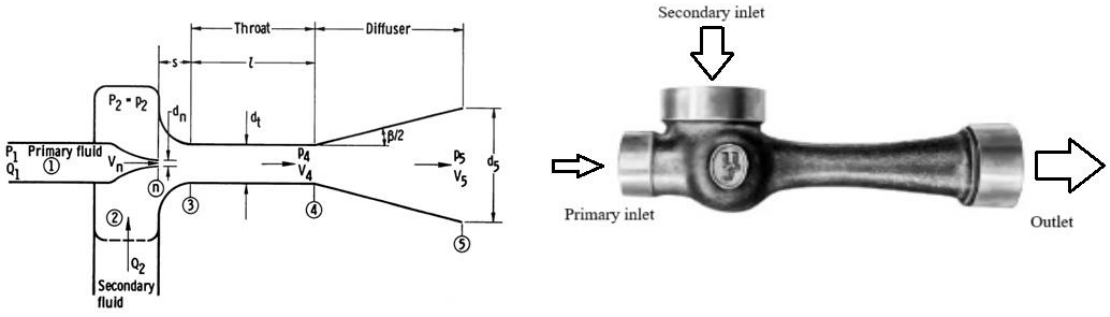

Fig. 1. Sections of a generic jet-pump – jet-pump

Note. Source [3], [4].

B. Statement of the problem

Based on the aforementioned variability and given that the performance of these devices is driven by complex fluid mechanics phenomena, it is necessary to implement selected and adaptable numerical models that can adequately predict the performance as well as the characteristics of the internal flow field.

There are simplified models based on the conservation equations, which predict particular or very general characteristics of the system; however, they fail to adequately capture all the phenomena, or they provide very limited information on the behavior of the physical properties throughout the jet-pump. Experimental designs, on the other hand, suffer from time-consuming and costly design, manufacturing, and testing processes, with no certainty about the correct or optimal performance of the system.

This is where Computational Fluid Dynamics (CFD) analysis provides a midpoint between accuracy, reliability and multiplicity of metrics and results, along with a fast and adaptable study process. However, there are aspects to be aware of in order to obtain proper results, these include the simplifications made, the compatibility of computational analysis, the used methods and their own considerations, among other points that will be addressed later in this text.

C. Justification

Considering the large amount of economic, time and personnel resources required for traditional prototyping, it results of interest to have models that allow to accurately estimate the performance of these devices in their different configurations. Without these predictions, determining the influence of each possible geometrical or operational change of the device would be a very complex trial and error experimental task.

Along with the progress in computational simulation, different analysis tools have been developed that obey different degrees of accuracy and computational cost. Among these, there are one-dimensional models that use the conservation equations of mass, momentum and energy to

predict characteristic values of the system, or CFD models that allow analyzing a greater number of internal properties and in many cases obtain a better accuracy of the pump performance[5], which usually involves a longer computational time, depending on the solution model, but it is worth it due to the improvement in the results.

For this reason, the simulation through CFD techniques is convenient, due to the level of detail, cost-effectiveness, and accuracy of the performance results. For this purpose, multiple cases are generated that can be contrasted with experimental results available in the literature, thus evaluating the usefulness of the simulation environment as a validated tool for predicting the jet-pump behavior during its design phase, and allowing the simulation of future configurations, in search of specific characteristics that best suit an application.

D. Objectives

This study aims to accomplish specific objectives which address significant aspects of the CFD simulations and the jet-pump performance evaluation. The general and specific objectives, functioning as specific goals and milestones of this research, are outlined.

1) General objective:

Develop computational fluid simulation components to accurately forecast the performance of a subsonic jet-pump, focusing on the prediction of key parameters including compression ratio, flow ratio, and energetic efficiency.

2) Specific objectives:

1. Establish a comprehensive reference framework by examining the historical background, antecedents, and conducting comparative studies of subsonic jet-pumps across diverse applications.

2. Build computational models of the pump geometry (CAD), considering different simplifications, dimensions, and design features, taking into account the computational analysis compatibility.
3. Conduct computational simulations to analyze the jet-pump performance across diverse operating conditions, systematically varying input parameters to assess their impact.
4. Analyze the simulation results for the different configurations, comparing them with relevant experimental data from existing literature.

E. Scope

This research focuses on the computational simulation, restricting the domain within the device, of the non-cavitational performance of a single-phase subsonic jet-pump, operating with water as fluid, for which different geometrical and operational configurations are considered. Based on the literature review, as will be discussed in the following section.

Given that, the NASA technical notes D-4759 and D-4445, elaborated by Sanger [1], [3], [6], are taken as a source of validation, since they provide great information on both the general performance and the internal flow of the jet-pumps; and that the maximum variability and error in results are typically observed at the points of maximum efficiency when comparing CFD models with experimental data, as addressed later. Consequently, it is decided to simulate the arrays with the best overall performance, adhering to Sanger's documented geometries and operating conditions in his experimental setups, as these are likely to naturally present the highest margin of error.

In Fig. 2 presented in Sanger's technical notes, the relationship between nozzle spacing, area ratio, throat length, and maximum efficiency is illustrated. From which the cases to be simulated are determined.

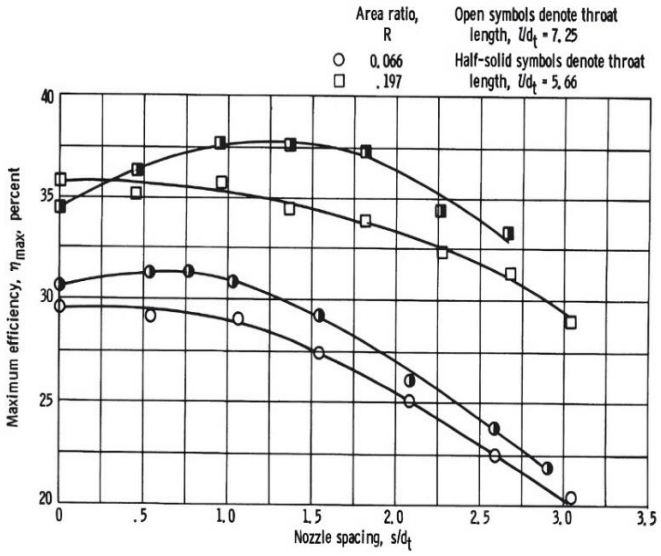

Fig. 2. Relationship between design parameters and maximum efficiency.

Note. Source [6].

Accordingly, this research considers:

- Throat length ratio of 5.66 throat diameters.
- Nozzle-to-throat area ratio of 0.197.
- Three positions of the primary nozzle relative to the throat's beginning, corresponding to the minimum, best efficiency, and maximum locations.
    - 0 throat diameters.
    - 1.36 throat diameters.
    - 2.66 throat diameters.

Regarding the operational conditions, eight flow ratios are simulated for which the general efficiency of the jet-pump is compared. Particular attention is given to the 1.4 and 1.6 FR, where the highest efficiency is achieved, and the pressure coefficient C_p and the total pressure flow field are analyzed.

In the simulations, due to licenses availability, ANSYS Fluent® is used for RANS-based turbulence modeling, following an incremental approach in terms of computational cost, until the simulation environment is considered validated, according to the available experimental data.

F. Chapter outlines

After introducing the conducted research and presenting its objectives, motives and scope, this work is organized in 5 additional chapters. Chapter II provides a concise review of the literature, discussing the background of jet-pumps and analyzing the existing models, experimental arrangements and previous studies that have been conducted.

Subsequently, Chapter III focuses on the problem's modeling approach and the computational models that support the related simulations. Following this, Chapter IV, presents the computational setup, detailing the conditions, the arrangements, and the way in which they are simulated.

In Chapter V, the results of the simulations and their respective analysis are presented, where the general performance of the jet-pump and the internal flow field are observed. This analysis sets the stage for Chapter VI, which discusses the key findings of this work, some future perspectives, and provides recommendations concerning this research.

A complementary article, which will be presented and published in the proceedings of ENFHT 2024 - 9th International Conference on Experimental and Numerical Flow and Heat Transfer, London, United Kingdom in April 2024, is included in the annexes [7].

II. LITERATURE REVIEW

A. Jet-pumps overview

Jet-pumps, also known as ejectors[1], are fluid dynamic devices that exchange energy between a high-energy primary fluid and a low-energy secondary fluid [1], [8]. This interaction affects the physical state of the entire system, resulting in several properties that are useful in multiple fields.

The primary fluid, which is at a higher velocity and pressure than the secondary fluid, is guided through the converging subsonic nozzle, due to the conservation properties, the velocity increases, and a transition from static to dynamic pressure is observed. Once this primary fluid is discharged into the mixing throat, a lower pressure zone is created compared to the secondary fluid, and this gradient causes the secondary fluid to be suctioned into the mixing throat through the device. For this reason, it is common to refer to the primary fluid as the motive fluid and to the secondary fluid as the driven fluid. It is important to note that the reason why the secondary chamber is closed, as opposed to an air amplifier, is to be able to incorporate specific substances into the mixture, as is the case with the airbrush.

In Fig. 3, a generic static pressure contour of the jet-pump can be observed, in a two-dimensional representation taking advantage of the axisymmetric condition of the device. There, it is shown how the motive fluid experiences a reduction in the static pressure as it advances through the nozzle, and that once it is discharged into the mixing throat, it produces a lower pressure than the one found in the secondary inlet, which is why it is admitted to the throat. At the end of the throat the diffuser is located, where the opposite process of the nozzle takes place, meaning that the velocity is reduced, and the static pressure is increased to an intermediate point between the pressures in the primary and secondary inlet.

Complementarily, Fig. 4 shows the typical change in fluid velocity through the nozzle and the way in which the secondary fluid is also accelerated in the inlet duct due to the suction, as well

[1] Jet-pump is used to describe a liquid-liquid ejector.

as the sections along the device. At the diffuser, the deceleration of the fluid is evidenced as mentioned above.

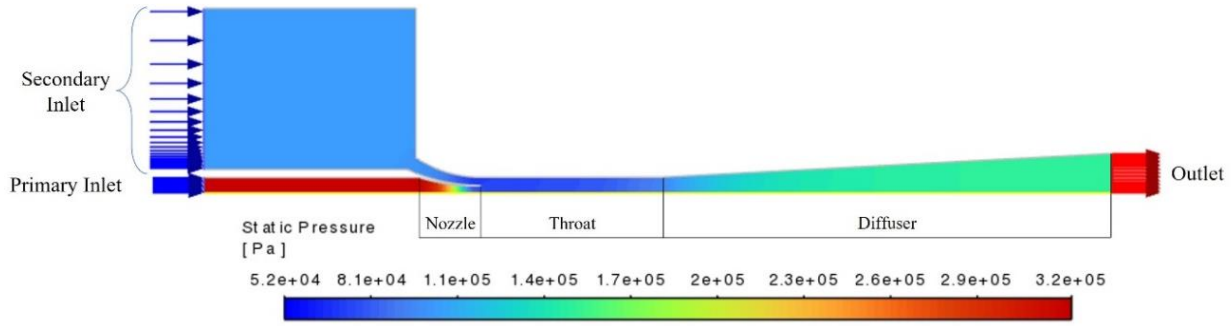

Fig. 3. Static pressure contour – generic representation.

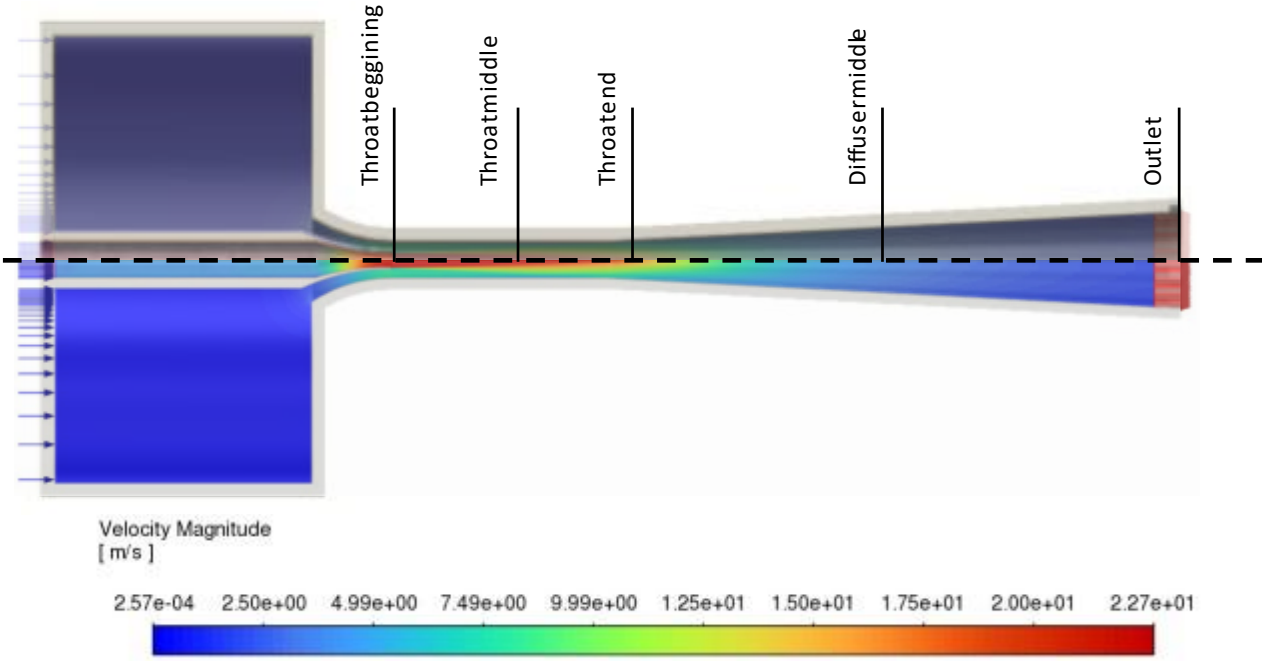

Fig. 4. Static pressure contour – generic representation.

In the throat, an exchange of energy takes place between the two fluids caused by turbulent phenomena, which naturally leads to the mixing of the two substances. Below, in Fig. 5, a generic turbulent kinetic energy contour is presented, which gives an idea of the interaction and mixing of the fluids along the throat and the diffuser, as a result of the internal velocity fluctuations.

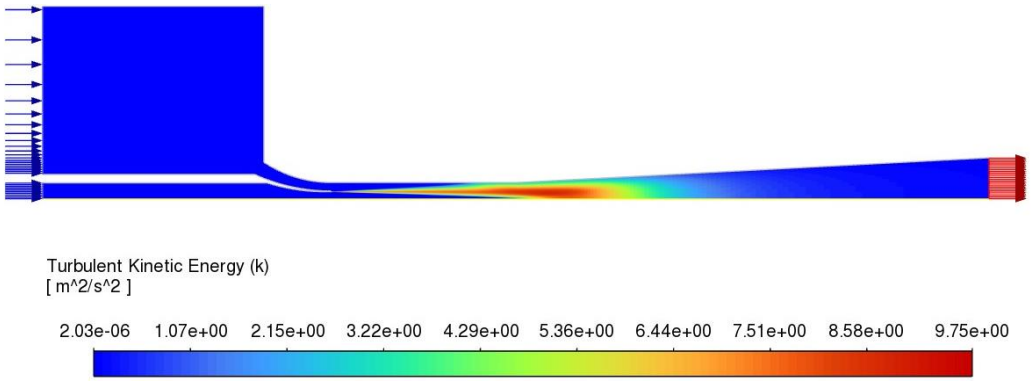

Fig. 5. Turbulent kinetic energy contour – generic representation.

Additionally, other ways to indirectly visualize the progress of the mixing process in different cross-sections along the jet-pump exist, through the value of physical quantities such as pressure or velocity, among others, since they are initially different but progressively become uniform, an example of this can be seen in Fig. 6,where the velocity profiles are plotted in vertical planes at the nozzle tip, in the middle of the throat, and in the middle of the diffuser.

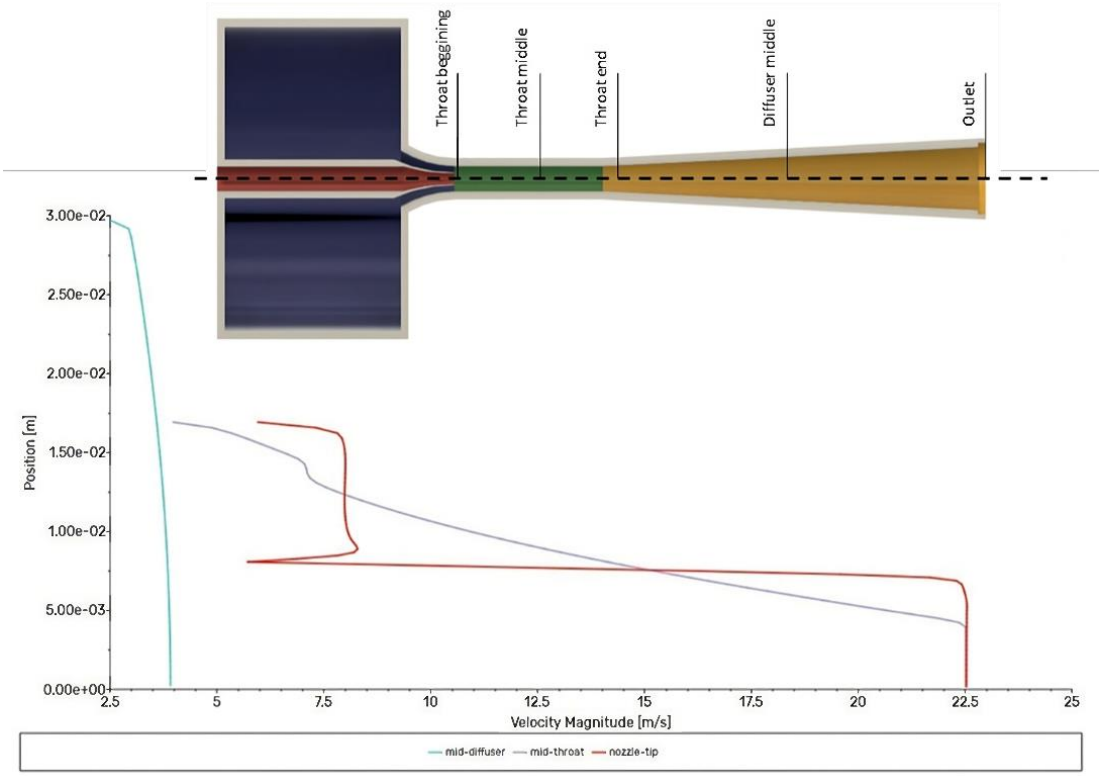

Fig. 6. Velocity profile in cross-sections – generic representation.

B. Performance parameters

This mixing process can be completed along the entire length of the throat, a case where the pump is called on design condition given its high efficiency, or it can continue across the diffuser, where it is named off-design condition because it presents an accelerated loss of efficiency.

The efficiency (η) is one of the characteristic non-dimensional parameters of a jet-pump, it is defined as the net power output divided by the net power input, or otherwise as the multiplication between the secondary to primary flow ratio (FR) and the pressure ratio (PR), as presented in [3]. The equations describing these variables are presented below, where subindex (1) represents the primary input and subindex (2) the secondary input:

$$FR = \frac{\dot{m}_2}{\dot{m}_1} = \frac{Q_2}{Q_1} \quad (1)$$

$$PR = \frac{(P_{out} - P_2)}{(P_1 - P_{out})} \quad (2)$$

$$\eta = FR * PR \quad (3)$$

Other common dimensionless parameters are the area ratio between the nozzle and the throat (A_r), parameter that influences the efficiency as can be seen in Fig. 2,Fig. 2. Relationship between design parameters and maximum efficiency. and the pressure coefficient (C_p), a metric directly related to the pumping effect, that allows the comparison between different operational conditions, i.e. values of FR and P_2. For the last one and according to Sanger [3], the upper part of Equation 5 is associated with the pressure increase, with respect to P_2, at any point along the jet-pump (P_x), while the lower segment accounts for the velocity head, meaning the fluid kinetic energy per unit weight at the nozzle tip.

$$A_r = \frac{A_{nozzle}}{A_{throat}} \quad (4)$$

$$c_p = \frac{P_x - P_2}{\gamma \frac{Vn^2}{2g}} = \frac{P_x - P_2}{\frac{\rho * Vn^2}{2}} \quad (5)$$

Once this general overview about jet-pumps has been given, multiple models that have been implemented to represent the performance of these devices are reviewed, together with the conditions and simplifications that have been used in them. Then, experimental arrangements are discussed, serving both as research tools and data sources for the validation of the models, for which the setups, the data collection method and the possible associated errors are examined. Finally, previous computational simulation studies and the special considerations involved in each of them, according to the respective research objectives, are analyzed.

C. Previous research

Numerous ways of predicting and testing the performance of jet-pumps have been documented in the literature. Theoretical models refer to those that work by using the conservation equations in their integral form, while numerical analysis involves the subdivision of the domain into smaller elements, the discretization of the same equations in their differential form and the application of computational methods to solve them in an approximate manner. Complementary to these, experimental setups are configurations and procedures designed to conduct physical experiments in order to obtain empirical data and, from these, validate the theoretical and numerical models.

1) Theoretical models

There are two main approaches for theoretical models in the literature. The first one, based on the models developed in [9] - [12], where two one-dimensional models for jet-pumps are compared with the experimental results in [1], assuming incompressibility and equal density of the fluids, that the edge of the nozzle coincides with the beginning of the throat, the nozzle wall thickness is zero, and total mixing at the end of the throat is achieved. Friction losses, considered by means of loss coefficients based on the pressure drop per segment, are what differentiate both formulations. The first one assumes friction losses considering a turbulent and fully mixed flow for the whole length of the throat, while the second one, referred as modified analysis, tries to include the development of the mixing profile to determine the friction loss coefficient.

Both models have as input the parameters FR, A_r, and the loss coefficients (K), and are solved for PR, thus allowing the calculation of η. Following are the adapted equations (6, 7) to maintain the notation used in this work, in these the terms K_p, K_s, K_t and K_d, correspond to the primary nozzle, secondary inlet, throat and diffuser respectively, and the terms K_t' and K_t'' are the descriptors of a mixing flow and a fully mixed stream, as corresponds.

Turbulent and fully mixed flow formulation:

$$PR = \frac{2A_r + \frac{2(A_r^2)(FR^2)}{1-A_r} - (1 + K_t + K_d)(A_r^2)(1+FR)^2 - (1+K_s)\frac{(A_r^2)(FR^2)}{(1-A_r)^2}}{1 + K_p - 2A_r - \frac{2(A_r^2)(FR^2)}{(1-A_r)} + (A_r^2)(1+FR)^2(1+K_t+K_d)} \quad (6)$$

Mixing profile formulation:

$$PR = \frac{2A_r + \frac{2A_r^2FR^2}{1-A_r} - (1 + K_t' + K_t'' + K_d)(A_r^2)(1+FR)^2 - (1+K_s+K_t')\frac{A_r^2FR^2}{(1-A_r)^2}}{1 + K_p - 2A_r - \frac{2A_r^2FR^2}{(1-A_r)} + (A_r^2)(1+FR)^2(1+K_t'+K_t''+K_d) + K_t'\frac{A_r^2FR^2}{(1-A_r)^2}} \quad (7)$$

The results obtained there showed that, although they were similar, the simplified model (Equation 6) fitted better to the experimental data. At the point of best performance, the error was around 3% of efficiency. Fig. 7 shows the comparison for two different A_r and a non-throat-spaced nozzle.

A similar study was performed in [13], [14], where analogously the theoretical and experimental performance of a liquid-gas ejector is compared, which requires that the formulation contemplates that part of the momentum exchange between the fluids results in the compression of the gas. Consequently, the proposed model, which deals with static pressure changes across the different sections, and which is based on one-dimensional continuity and momentum relationships, acquires a quadratic or cubic nature and, therefore, results in a more complex analysis, facilitated through the use of computational tools.

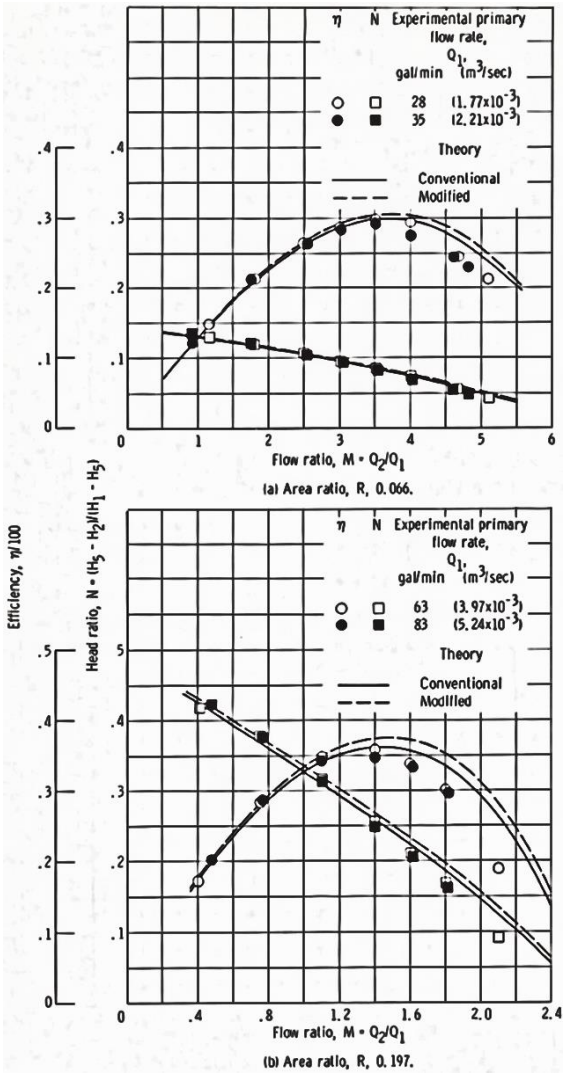

Fig. 7. Comparison of theoretical models with experimental results for different A_r.

Note. Source [3].

Said work showed that the model adequately predicted gas compression and energy losses in the throat and the diffuser, and that if coupled with an energy analysis and an optimum throat length approach, it would provide valuable information for the design of liquid-gas pumps. Furthermore, it was determined that the efficiency of these devices is highly dependent, among other losses, on those produced by energy dissipation during the mixing, due to the interaction between phases with different velocities.

The second approach, focused on the modeling of jet-pumps operating with a gas and a liquid (water in this case) as fluids, is the one described by Ravan Ghalati in [8], in which a one-

dimensional model based on the conservation equations of mass, momentum and energy is applied to on-design and off-design conditions, by decomposing the device into its components. For each of these, the corresponding equations are established to determine the compression ratio and the total efficiency of the device, and then they are compared with experimental results from the literature. The presented methodology demonstrated the ability to adequately predict the pump behavior under diverse conditions, considering the pressure ratio (PR) and efficiency (η). Specifically, under on-design conditions, the method exhibits a remarkable accuracy, with a performance error margin below 5%; on the other hand, the off-design condition presents a maximum of 9% for the pressure ratio and 23% for the efficiency, these results can be seen in Fig. 8.

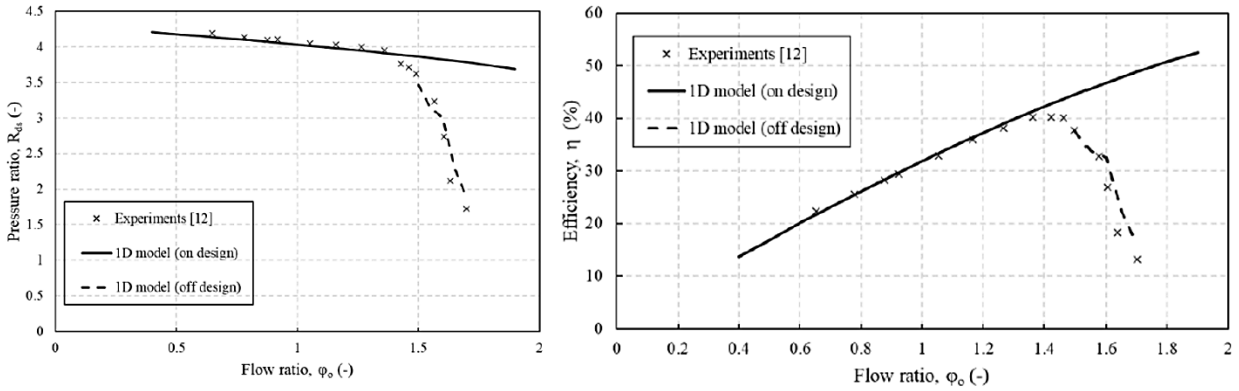

Fig. 8. Comparison of 1D models – On-design and off-design conditions.

Note. Source [8].

As it has been seen, theoretical models result from different applications and simplifications of the conservation equations, depending on the case and phenomenon under study. Therefore, the adaptation of the postulations of other authors is a recurrent practice, considering some particular factor or parameter that accounts for a certain condition of interest. This is the case of [15], [16], where the first one proposes a form with equal pressure of both fluids at the mixing section inlet, this implies a simpler model, where it is not required to know in advance pressure and velocity data, as long as some geometrical aspects of the jet-pump are present. The adapted model [16] is closer to the real behavior, it respects the inequality of pressures, adding a degree of complexity but improving the accuracy, provided that the necessary data is available.

In summary, the theoretical models described above play a crucial role in understanding jet-pump performance and are valuable tools for their design. However, it is notorious that the simpler the model, the lower the accuracy of it, and in the opposite case, it is usually required to couple these formulations with data from analysis through computational tools or already known values.

Given that it is common that these models are developed simultaneously with experimental studies or are compared with data from the literature. We proceed to the review of some instrumentation and results, commonly used as a validation mechanism, both for the analytical and numerical proposals.

2) Experimental setups

Numerous experimental arrangements exist to investigate different characteristics or applications of jet-pumps. Among these, some operate with the combination of two different fluids, as is the case of [13], [14], systematically studying the influence of geometry, jet velocity and suction pressure on the performance and behavior of these pumps. To achieve different throat lengths and allow the study of the flow, transparent blocks are used, which are attached to a conical diffuser with an angle of 5.4 degrees, the interchangeable nozzle also allows sliding along the pump axis to regulate the throat spacing. Static pressure sensors are located from the throat forward, and the flow rate and inlet pressure are measured and regulated. Finally, they present the comparison with one of the theoretical models previously discussed and suggest a design criterion on the ideal throat length in design cases. The results of the investigation can be seen below in Fig. 9.

Investigations such as [17] or [18], both working with liquid-gas interactions, present experiments designed to study the applicability and optimal performance in industry applied cases. In the first one, the problem of freshwater demand is considered, for which the use of jet-pumps as desalination tools is proposed. There, a variable geometry device is designed, measuring the inlet pressure and flow rate for both fluids, vacuum pressure, and outlet pressure, from which the pressure ratios and efficiency under different operating conditions are reported.

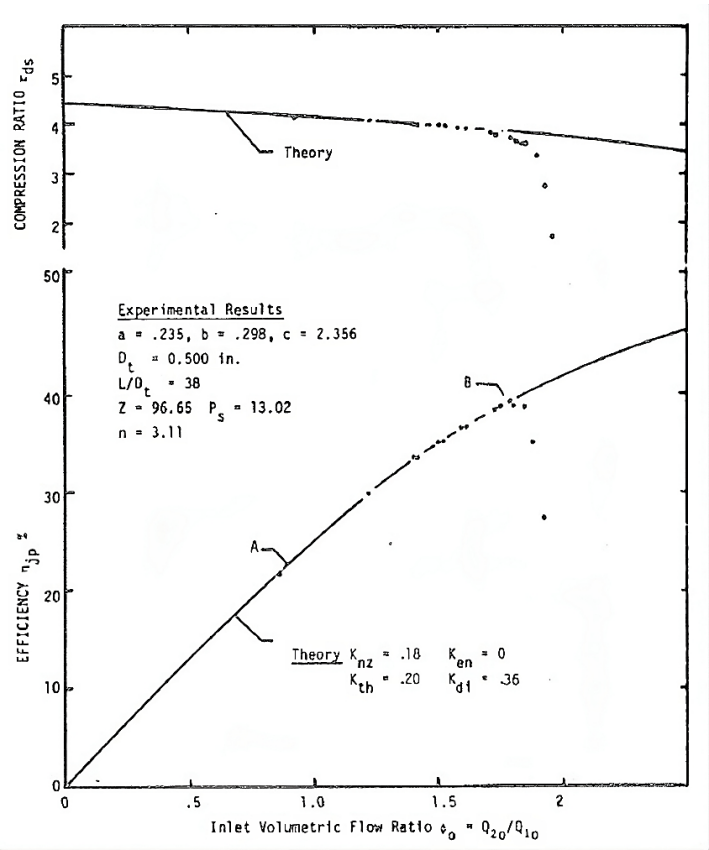

Fig. 9. Results of the experimental-theoretical study.

Note. Source [14].

In the second research, the use of steam jet-pumps is studied, for the transport of radioactive materials and hazardous liquids, these have the particularity that both the primary inlet and the throat are convergent-divergent nozzles, for which a special arrangement is developed, where steam is used as motive fluid and water is pumped (simulating the substance). Similarly, inlet flow rates, static pressure and temperature are monitored longitudinally, to compare with numerical models implemented at the same time.

Regarding liquid-liquid jet-pumps, [19] shows the development of a system to increase the flow rate in nuclear applications. The system, shown in a representative schematic in Fig. 10, is equipped to measure the usual parameters of pressure, temperature, and flow rate, to generate results where the ratio of pressures and efficiency is contrasted with respect to different design characteristics.

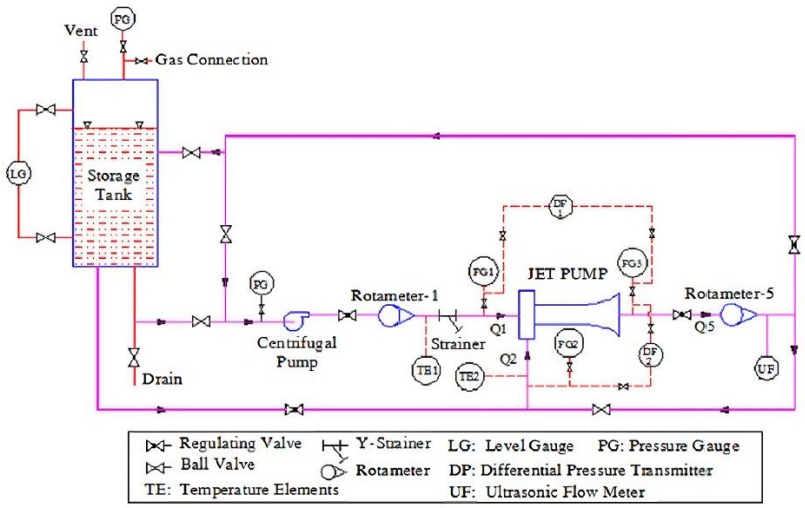

Fig. 10. Schematic representation of the test bench.

Note. Source [19].

In the case of [15], water is used in both inlets and the effects of A_r and the nozzle cross-sectional shape are studied, including circular, triangular, and square geometries. It is found that for the arrangement used, the circular nozzle gives the best performance, and the best area ratio is approximately 0.30, this through the common PR and η plots analysis. Moreover, in [20] an axisymmetric jet-pump (circular section at all points) is used, also employing water-water, and where the primary flow pressure and the spacing of the nozzle to the throat are variable, parameters whose affectation to the performance are the objective of this study. In addition to efficiency and pressure ratio, static pressures on the outer wall and velocity along the apparatus are documented.

A noteworthy case, as mentioned in the scope of this paper, is the one presented by Sanger in [1], [3], [6]. He develops numerous experimental tests using a jet-pump, resulting from the optimization of his own previous work, which has a throat length equal to 5.66 D_t, circular cross section, variable position of the primary nozzle, and interchangeable nozzles with area ratios of 0.197 and 0.066. Three total pressure sensors are installed at 2.6, 4.8 and 10.4 D_t from the start of the throat and 18 static pressure taps are installed along the length of the device. Furthermore, there is a high accuracy reading and control of the air content in the mixture (less than 3 parts per million), pressure, flow rate and temperature, both for the individual inlet flows and for the mixed fluid. The characteristic dimensions of this design can be seen in Fig. 11, whose units are expressed in inches (centimeters) or throat diameters for the location of the sensors.

The tests are performed separating the cavitational and non-cavitational operation, for the latter case, since it is the one of interest in this study, a constant absolute pressure in the secondary inlet of 1.03×10^5 N/m^2 is used, and the primary flow rate and the nozzle spacing are varied in the different runs. The overall performance is presented with the efficiency and pressure ratio metrics as usual, the effect of the flow rate, nozzle spacing and area ratio is analyzed for these, and compared with the results of the previous study, from which the device was optimized. A special feature is that for the most efficient FRs, the pressure coefficient profiles (calculated from the static pressure) and the normalized total pressure at the cross sections where the respective sensors were located are recorded, providing valuable information about the internal flow field.

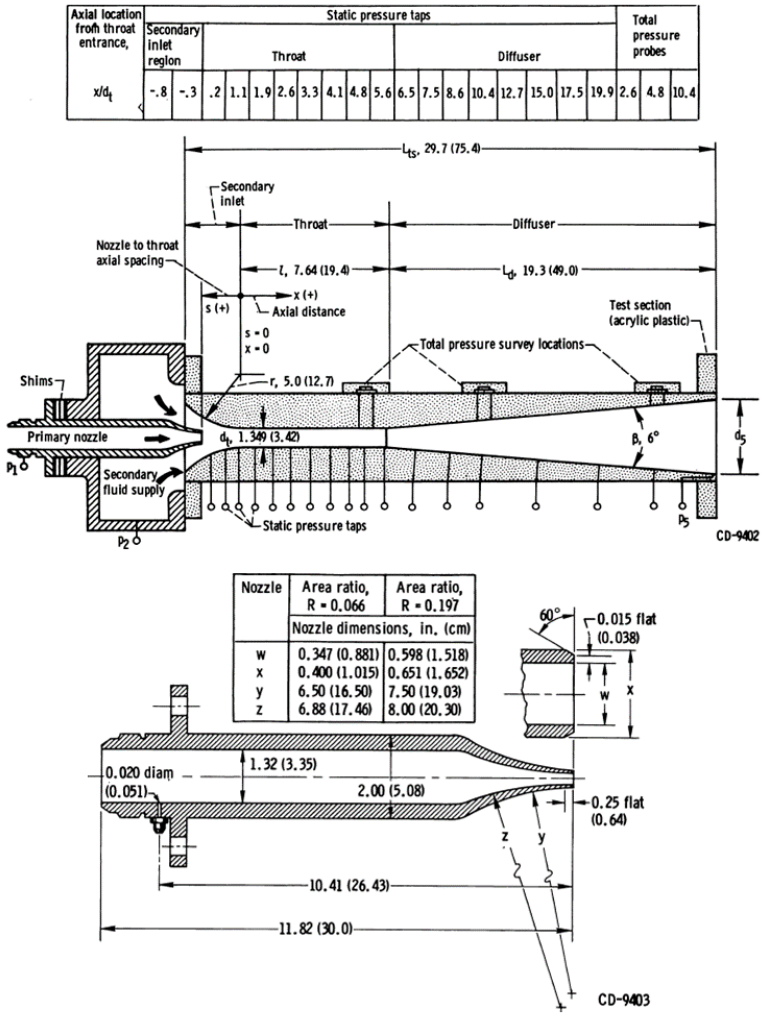

Fig. 11. Schematic representation of Sanger's jet-pump – Units in inches (centimeters).

Note. Source [6].

The results obtained by Sanger indicate that the area ratio of 0.197 achieved better overall performance. Within this characteristic, the spacing of 1.36 Dt reached the highest efficiency with 37.6% corresponding to a flow ratio of 1.6 and a pressure ratio of 0.233. Given this, the results of the pressure coefficient with respect to jet-pump length for different spacings and flow ratios of 1.4 (second best performance) and 1.6 are available, in addition to the normalized total pressure for the three cross sections with a FR of 1.6.

The maximum efficiency is reached in accordance with the theory, as the flow ratio increases and the mixing zone moves towards the end of the throat, in the case of continuing through the diffuser, the expansion losses cause it to decay rapidly and therefore the efficiency curve describes a parabola. In relation to the performance equations presented above, it is evident that as the flow ratio increases the pressure ratio decreases, which is due to the ability to transform kinetic energy of the primary input into a compression effect.

Since the Sanger works concerning the design and testing of jet-pumps [1], [3], [6] are very well documented, it is decided to use these data as a validation source for the simulations contained in this work, as many other studies have done due to its relevance in the literature. As previously noted, the points of higher efficiency are usually the ones of greater discrepancy between empirical measurements and numerical simulations, this is why the characteristics outlined in the scope (Chapter I, Section E) are chosen as the limiting factors for this work. The Sanger results concerning these conditions are displayed in Fig. 12, Fig. 13, and Fig. 14, as reference for the subsequent chapters. It is important to mention that the instrumental and reading error estimated in these reports ranges up to a maximum of 5%, and that the plot points are obtained using the Web Plot Digitizer software [21].

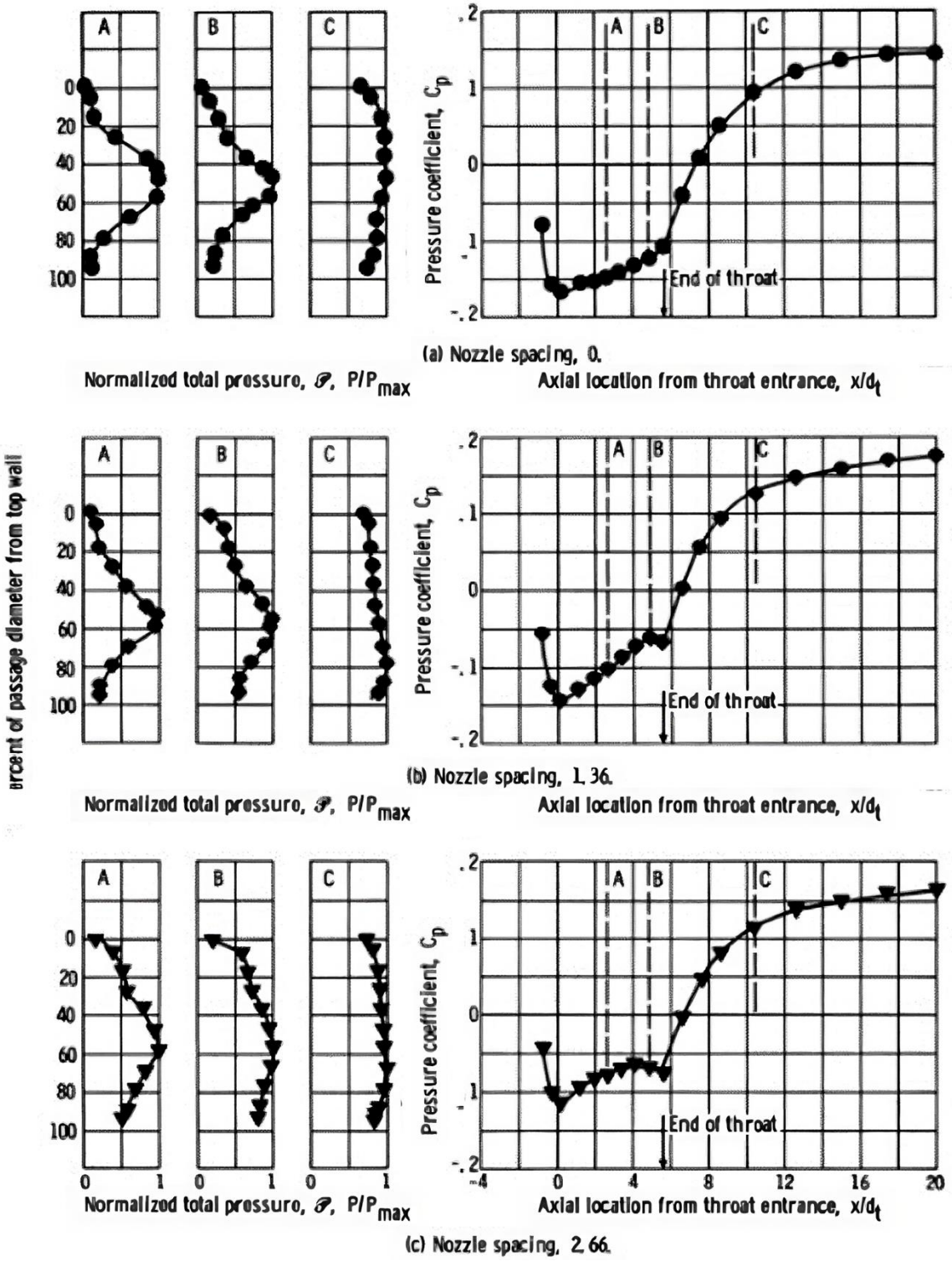

Fig. 12. Normalized total pressure and pressure coefficient for $0.197A_r$ 5.66 D_t 1.6FR.

Note. Source [6].

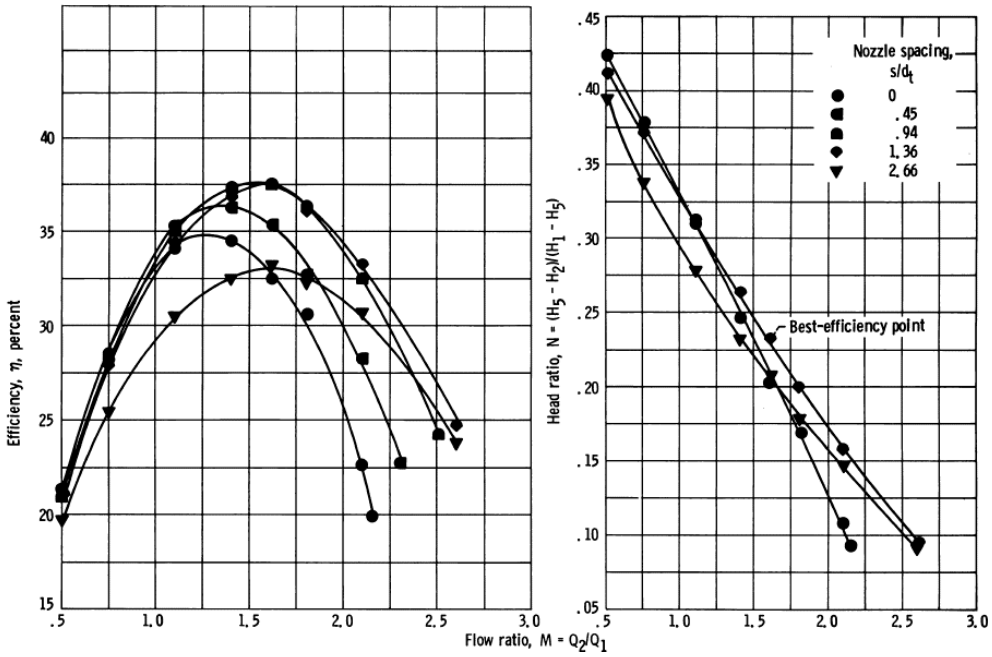

Fig. 13. Overall performance for $0.197A_r$ 5.66 D_t - Primary flow rate ($3.97x10^{-3}$ m^3/sec).

Note. Source [6].

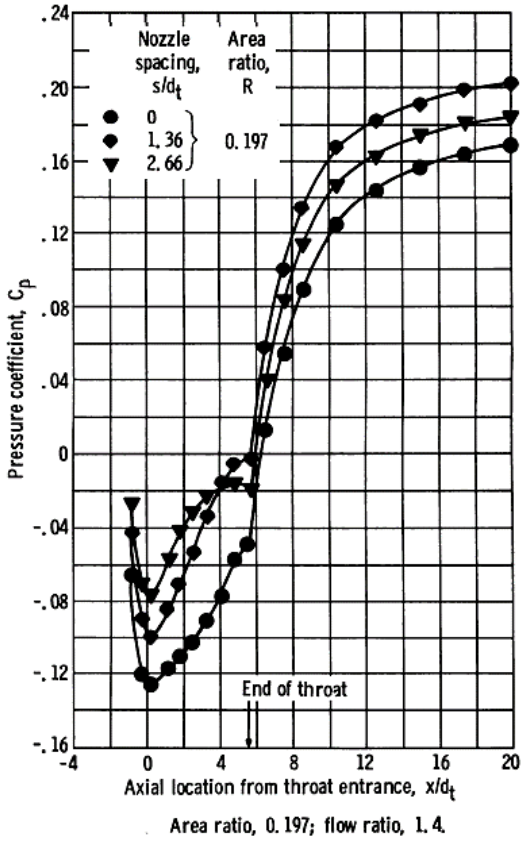

Fig. 14. Pressure coefficient along the jet-pump for a 1.4FR.

Note. Source [6].

3) Numerical analysis

Considering that theoretical models are very limited in the information they can provide about the behavior of jet-pumps and they usually require adjustment of the loss coefficients based on experimental information, and in contrast, experimental setups are expensive, slow and not very versatile; it is interesting to study the behavior of these devices using CFD analysis, since it allows modeling different designs and operating conditions in an agile and accurate way, providing relevant information about the overall performance and the internal flow field.

Among the studies that are conducted using CFD, it is common to find some studies that change geometrical characteristics or input parameters to observe their impact on the behavior of the device, such as the cases presented in [5], [22] - [24], among many others. A second area that is usually considered is to use different turbulent approaches in the analysis and contrast the results obtained with empirical data, these approaches vary the form and scale in which they consider the eddies of the flow, which incurs in the computational cost of each simulation as can be seen in Fig. 15, where Direct Numerical simulation (DNS) is the most demanding, followed by Large Eddy Simulation (LES) and finally, Reynolds-averaged Navier-Stokes (RANS) as the least requiring approach[25].

Generally, DNS simulations of ejectors are not used due to the very high computational cost, however, hybrid DNS/LES or DNS/RANS models have been proposed, such as the one presented in [26], where the lower computational cost model is proposed for the majority of the jet-pump and the DNS for the mixing zone. Regarding LES simulations, these have been used in some detailed studies, for example in [27], [28] they analyze the flow characteristics by means of this type of simulations, or in [29] where the behavior and the cavitation phenomenon are predicted. In both cases, it is noticeable the significant computational cost required, as it is expected in this type of simulations, therefore their versatility is very limited, and they may be used for a more detailed design or the analysis of a very particular aspect.

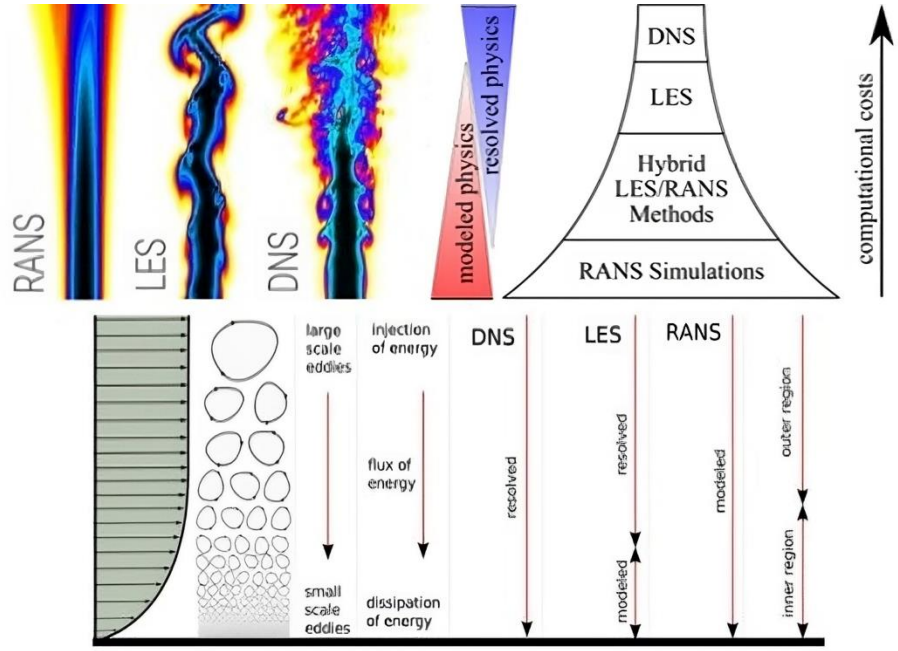

Fig. 15. Turbulence modeling approaches.

Note. Source [25], [30], [31].

In this context, RANS simulations provide the fastest and, even though less detailed, sufficiently accurate alternative for most of the study phenomena, which is why they are the most widely used in the literature and their results are usually considered acceptable. For example, in [32], [33]the performance of jet-pumps under different turbulence models is analyzed and the performance of multiphase jet-pumps for gas compression is modeled, respectively. Giving an idea about the applicability of these simulations for both single-phase and multiphase cases.

Finally, in [16], axisymmetric simulations combined with a one-dimensional model were performed to determine the friction loss coefficients for each section of a jet-pump. In this process, the k-ε, k-ω, and k-ω SST turbulence models were used, and it was determined that the k-ω SST was the one that best captured the fluid dynamic phenomena of the device, mainly at the points of maximum efficiency. Complementarily, in [23], simulations were run for a pump with distillation and desalination applications. In this study, they decided to use the standard, realizable, and RNG variants of the k-ε method in order to find the one with the best accuracy. Additionally, they indicate the use of ANSYS Fluent® as solution environment, the simple velocity-pressure coupling method and the use of scalable wall functions. Subsequently, during the validation, they find a

higher affinity with the standard model, followed by the realizable, and finally the RNG, as shown in Fig. 16.

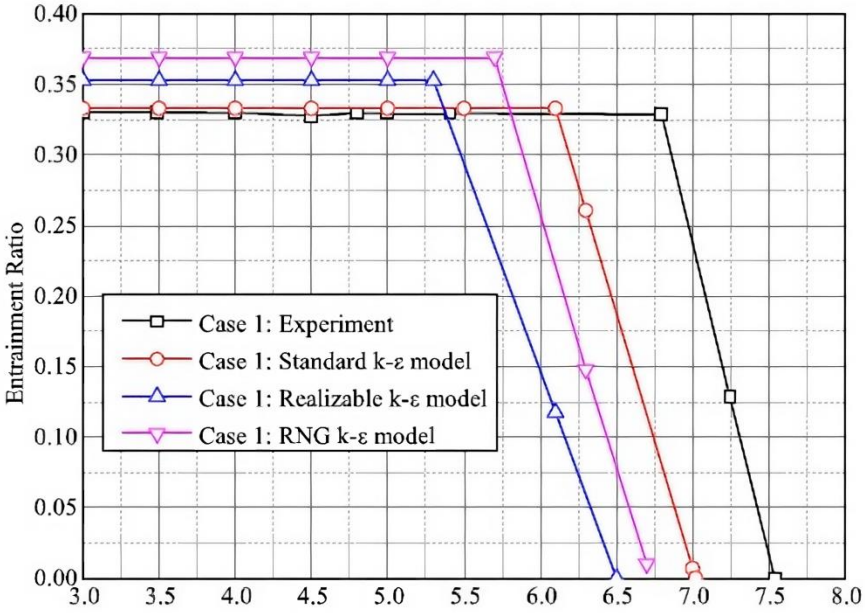

Fig. 16. Validation results with own device for k-ε models.

Note. Source [23].

Throughout this chapter, the progress of the study of the behavior of jet-pumps has been explored through different models and arrangements available in the literature, covering analytical, experimental and, finally, CFD numerical analysis approaches. Through this review, it is possible to understand some of the advantages, disadvantages, and particularities of each of these areas of study. These aspects are essential since they provide important considerations and limitations to be taken into account for the development of this research. Additionally, they establish the framework for the following chapter, where the methods and models supporting the computational simulations for this application are presented.

III. SUPPORTING MODELS

A. RANS approach

As previously stated, the RANS approach provides the necessary accuracy and versatility requirements for most applications where the generic behavior of a system is to be studied. This approach simplifies the Navier-Stokes (N-S) equations, which describe the behavior of viscous fluids, so that turbulent flow can be modeled with relative ease.

For this, the Reynolds decomposition is applied, where instead of studying the field of properties in its unsteady and time varying nature, it is modeled for the averaged profile, by separating the time averaged components and their corresponding fluctuation. An example of how these profiles are averaged can be seen in Fig. 17, there the velocity profile (black line), is averaged over time resulting in the red line ($\bar{u}$), while the component (u') represents the velocity fluctuations [34]. By taking this decomposition to the N-S equations, averaging them, and adding certain closure equations, a simplified set of equations is obtained, which provides general information about the system and does not require a computing power as large as the DNS and LES approximations.

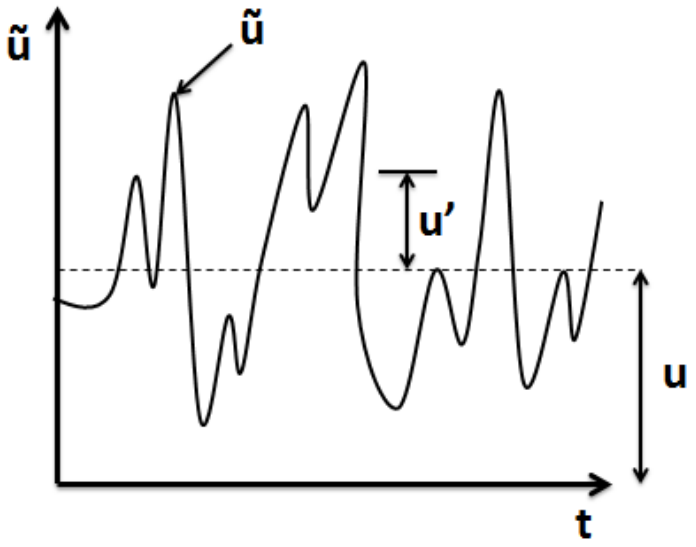

Fig. 17. Reynolds decomposition for a velocity profile.

Note. Source [34].

In detail, the starting point is the N-S equations in their stationary and incompressible form (Equations 8 and 9). These equations respectively correspond to the continuity of mass and momentum. As these are described in an x,y,z coordinate system, the components u,v, and w, are used to refer to the flow in that reference frame, respectively.

$$\nabla \cdot u = 0 \quad (8)$$

$$\frac{\partial u}{\partial t} + (u \cdot \nabla)u = -\nabla p + \frac{1}{\mathrm{Re}} \nabla^2 u \quad (9)$$

To these, the Reynolds decomposition described in Equations (10 - 12) is applied, where the first one is the generalization of it and Equations 11 and 12 are the components in terms of a mean flow and the associated turbulent fluctuations.

$$u(x,t) = \bar{U}(x) + u'(x,t) \quad (10)$$

$$\bar{U}(x) = \lim_{T \to \infty} \frac{1}{T} \int_0^T u(x,t)\, dt \quad (11)$$

$$u'(x,t) = u(x,t) - \bar{U}(x) \quad (12)$$

With this replacement and averaging over time, Equation 13 is obtained from Equation 9. The first three terms remain the same, since the average of an average is invariant, and the remaining terms become 0, given the fluctuating terms definition. Consequently, Equations 14 and 15 are obtained, which indicate that the divergence of both the mean flow and the fluctuating components is equal to zero.

$$\overline{\frac{\partial}{\partial x}\bar{U}} + \overline{\frac{\partial}{\partial y}\bar{V}} + \overline{\frac{\partial}{\partial z}\bar{W}} + \overline{\frac{\partial}{\partial x}u'} + \overline{\frac{\partial}{\partial y}v'} + \overline{\frac{\partial}{\partial z}w'} = 0 \quad (13)$$

$$\overline{\frac{\partial}{\partial x}\bar{U}} + \overline{\frac{\partial}{\partial y}\bar{V}} + \overline{\frac{\partial}{\partial z}\bar{W}} = \nabla \cdot \bar{U} = 0 \quad (14)$$

$$\overline{\frac{\partial}{\partial x}u'} + \overline{\frac{\partial}{\partial y}v'} + \overline{\frac{\partial}{\partial z}w'} = \nabla \cdot u' = 0 \quad (15)$$

Similarly, for the momentum equation (Equation 10), by replacing, averaging over time, and performing some mathematical simplification procedures, such as the application of the identity described in Equation (15), three equations are obtained, corresponding to the different components. However, these can be grouped as shown in Equation 16, in this generalized form the indexes i = (1, 2, 3) are associated to (x, y, z) respectively.

$$\bar{U}_j \frac{\partial \bar{U}_i}{\partial x_j} = \frac{1}{\rho} \frac{\partial}{\partial x_j} \left(-p\delta_{ij} + 2\mu \bar{S}_{ij} - \rho \overline{u_i' u_j'} \right) \quad (16)$$

$$\bar{S}_{ij} = \frac{1}{2} \left(\frac{\partial \bar{U}_i}{\partial x_j} + \frac{\partial \bar{U}_j}{\partial x_i} \right) \quad (17)$$

As can be seen, both Equation 13, where the fluctuating components are made zero, and Equation 16, are expressed in terms of the mean flow, except for the term $\rho \overline{u_i' u_j'}$. This, referred to as Reynolds Stresses in the literature, represents the effects of turbulent fluctuations in momentum on the fluid and conversely. Furthermore, to close the system of equations and express everything in terms of the mean flow, it is necessary to model these stresses, being what is known as the closure problem.

To model the above-mentioned stresses under the Eddy Viscosity Models (EVM), the Boussinesq hypothesis can be used, which relates said fluctuations to the product of an eddy viscosity (ν_t) and mean flow quantities, as shown in Equation (18). Thus, it is necessary to model this eddy viscosity as a function of determinable values. This is where the different closures are used to simulate the behavior of the fluids in near-wall regions.

$$\overline{-u_i' u_j'} = \nu_t \left(\frac{\partial \bar{U}_i}{\partial x_j} + \frac{\partial \bar{U}_j}{\partial x_i} \right) - \frac{2}{3} k \delta_{ij} \quad (18)$$

Particularly, in this research the *k-ε* standard model is used, with standard, scalable, and enhanced wall functions; and the *k-ω SST* model, which is a composition of *k-ω* in the near-wall zones and *k-ε* in the rest of the domain.

These two closure models are based on the Turbulence Kinetic Energy (TKE) to define two partial differential transport equations allowing to determine the eddy viscosity and completing the system of equations. Particularly, for k-ε these two equations are the TKE (k) and the TKE dissipation rate (ε), as can be found in [35]; from which the eddy viscosity (ν_t) is calculated according to Equation 19.

$$\nu_t = \rho C_\mu \frac{k^2}{\varepsilon} \quad (19)$$

On the other hand, the *k-ω* model for the near-wall zones in *k-ω SST*, uses the same turbulence kinetic energy for the first equation, but the specific TKE dissipation rate (ω) for the second, detailed equations can be found in [36]. This is directly related to (ε) by Equation 20 and thus (ν_t) results as presented in Equation 21.

$$\omega = \frac{\varepsilon}{C_\mu k} \quad (20)$$

$$\nu_t = \frac{\rho k}{\omega} \quad (21)$$

Although both models are related, the difference between them resides in the behavior within the viscous sub-layer (proximity to the wall), where *k-ε* uses empirical damping functions in the coefficients attached to the (ε) terms, while *k-ω* does not require them. Nevertheless, the *k-ω* model has the disadvantage that it is very sensitive to changes in the freestream turbulence. Hence, the combined *k-ω SST* model manages to accurately capture the behavior near the wall and reduces the influence of the freestream turbulence over the result.

For *k-ω SST*, substituting into the dissipation equation of (ε) so that $\varepsilon = C_\mu k\omega$, results in the same equation as for *k-ω* but with an additional term. It is therefore possible to multiply this by the blending function $(1 - F_1)$; where $F_1=0$ yields in the *k-ε* model, $F_1=1$ in the *k-ω* model and any value in the middle in a smooth transition. These values are usually modeled by a hyperbolic tangent related to the distance to the nearest wall and, combined with the unification of the

empirical constants of each model through the same factor (F_1), smooth transition between closures in any cell and direction is achieved.

Finally, to obtain the *k-ω SST* model, a viscosity limiter is incorporated, since this still tends to overestimate the wall shear stress. This limiter resembles the previous blending function $(1 - F_2)$, and is incorporated into the eddy viscosity equation. By doing this, the value is not affected at a distance from the wall, but as it gets closer, the viscosity value becomes lower than the original, thus improving the results.

B. Numerical solver

In order to implement and solve these models, some additional steps and considerations are required to calculate the flow fields, discretize the mesh, assign the properties to the different cells, among others. For this reason, computational methods and techniques are used in the different software, both commercial and private, to adequately simulate each case. The corresponding elements that have been used in this research are presented below, as detailed in [37], [38].

This way, to solve the equations of continuity, momentum and turbulence, the finite volume method is used, where the domain is separated into controlled volume cells and the properties are calculated for the centroids of each of these, in what is essentially the discretization and linearization process.

Based on this, the gradients of the different variables are approximated by the least-squares gradient method, which uses a linear interpolation between adjacent cells to construct a matricial equation, from which the solution is approximated. For some terms that require the wall value of each cell, the value is interpolated from the centroids using a second-order upwind scheme, where it is derived from contiguous upstream cells in a multidimensional manner, achieving higher accuracy than the first-order schemes. Similarly, the Rhie and Chow method is used to calculate the mass flux through the cells, which manages to dampen the oscillations and instabilities that arise in the coupling and therefore improves the accuracy of the simulations.

Moreover, taking into account that the velocity and pressure fields are closely related and depend on each other for the convergence of the simulation, the so-called pressure-based solvers are used. These run an iterative process where, from the values of the fields at a previous instant or the initialization, they calculate a provisional velocity value to solve for the momentum equation. Subsequently, this velocity is incorporated into the pressure-based continuity equation, which is a transformation of these equations in function of the pressure. Based on this, the corrected fields are obtained, a process that is repeated until the convergence threshold is reached.

To perform the coupling between velocity and pressure, the SIMPLE algorithm performs a sequential process of solving the governing equations, unlike a Coupled algorithm that solves them simultaneously. With this, the pressure field is obtained by trying to force the conservation of mass by means of corrective terms that are added to the equations and in this way the cycle continues.

Finally, a method that solves the set of equations up to the user-defined convergence is required. For this purpose, the Gauss-Seidel method provides a simple and optimal alternative for systems with numerous equations. This method resorts to an iterative process, in which a solution seed vector is considered, and the components are continuously updated as the system is solved. Additionally, information from nearby components is incorporated, refining the model until it reaches the convergence requirements.

IV. COMPUTATIONAL SETUP

A. Setup overview

The simulation process involves the geometry development, meshing, solver configuration and finally the processing of the results. Under a Standalone-Software philosophy, different softwares are used for each of these steps and files are exported and imported as required. This allows to take advantage of the benefits that different programs can offer for each segment of the process without being limited to one software-bundle, to improve the organization of the workflow, and to modify files without affecting the subsequent dependencies.

In detail, the geometries for the simulations are created in the software Autodesk Fusion 360® version (2.0.16490) in accordance with the dimensions specified in the Sanger reports [6] and with the considerations stated in the scope (Chapter I, Section E). The meshing is performed in a structured way in ANSYS Meshing, aiming for good mesh quality and convergence. Then, ANSYS Fluent® 22.1 is used, initialized in 2D and with double precision, where the starting parameters are configured, the simulations are run, and the results are extracted.

B. Geometry design

The geometries are designed following the measures described in the drawings of the reports to be used as validation mechanism (Chapter II - Fig. 11). Three versions are generated with the same throat lenght ratio of 5.66 D_t and a nozzle-to-throat area ratio of 0.197, but with spacings between the nozzle-tip and throat entry of 0, 1.36 and 2.66 D_t.

Since this has an annular shape as can be seen in Fig. 18, the design is simplified to a two-dimensional axisymmetric version, reducing the number of cells to represent the domain, and thus shortening the simulation process. An example of the geometry is the one developed for the nozzle-spacing (nxp) of 0, which can be seen in Fig. 19.

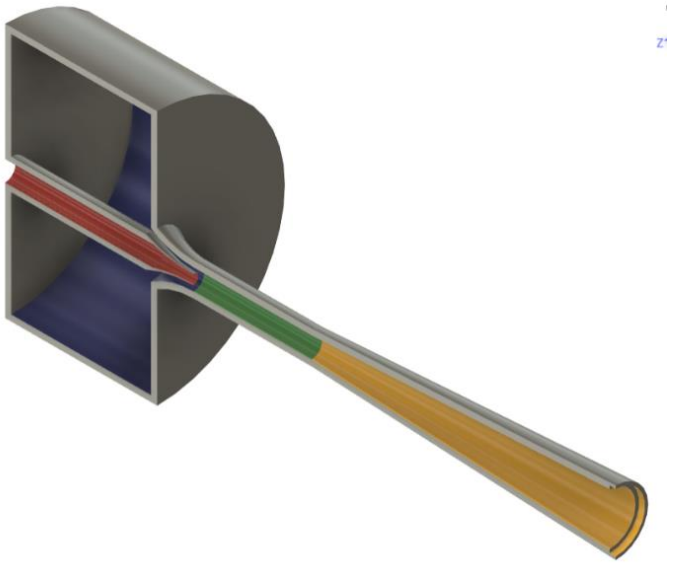

Fig. 18. CAD design – All units in (millimeters).

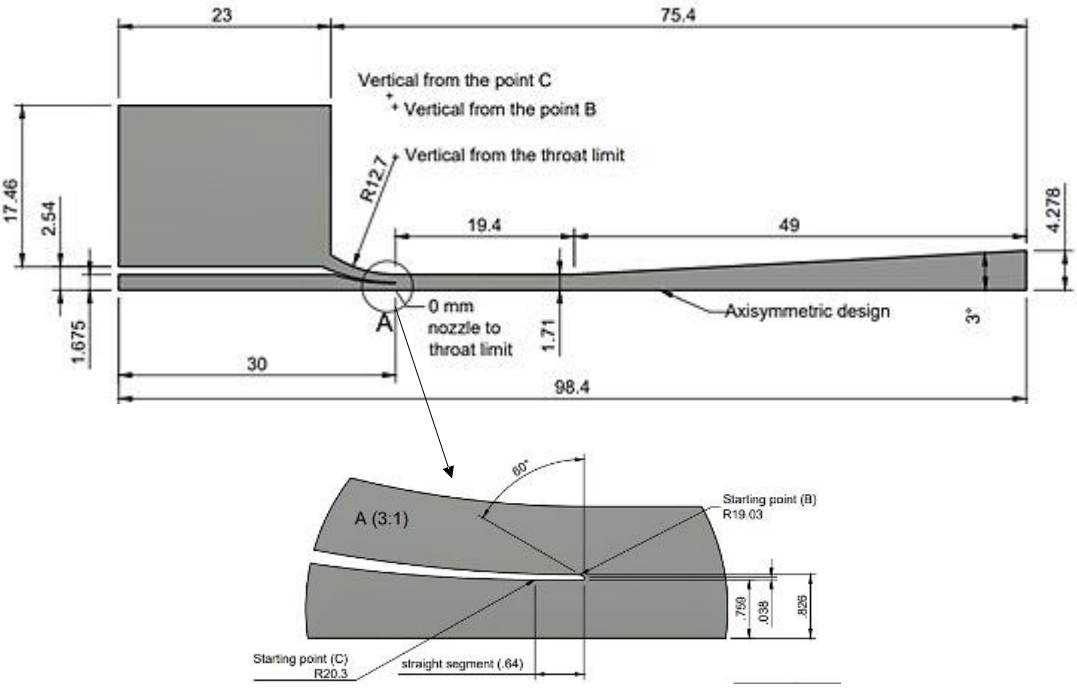

Fig. 19. Drawing of the jet-pump with a nxp of 0 – All units in (centimeters).

The other two versions of nxp's have the same dimensions for the nozzle-tip, the secondary chamber, the throat, and the diffuser; but the nozzle is retracted 1.36 and 2.66 D_t with respect to the throat entry. Fig. 20 shows the primary nozzle retracted 9.097 centimeters, which corresponds to the nxp of 2.66.

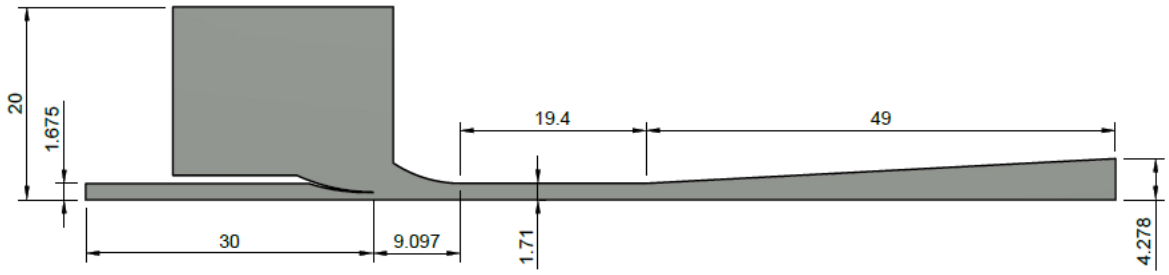

Fig. 20. Drawing of the jet-pump with a nxp of 2.66 – All units in (centimeters).

As a last step of this subprocess, these surfaces are divided into differentiable zones for the meshing software. This is done to reduce the number of cells in areas where properties do not vary much, avoid large area jumps between elements, minimize the number of curved or deformed cells, and thus achieve a structured rectangular mesh with good quality parameters, such as aspect ratio, orthogonality, skewness, among others. An example of how the jet-pump geometry is segmented is presented in Fig. 21, where the version with a nxp of 1.36 D_t is divided according to the projections of the contour vertices.

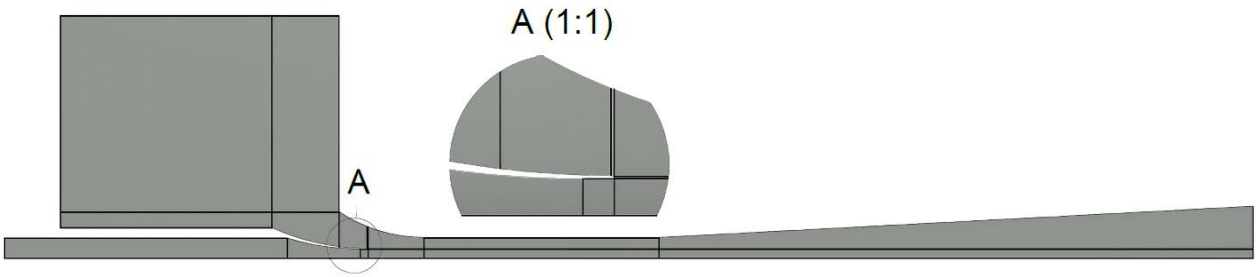

Fig. 21. Drawing of the jet-pump with a nxp of 1.36 – Zonal partitioning.

C. Meshing

Taking into account the geometry and its respective divisions, the most critical regions for the mesh are determined, i.e., areas where, due to the geometry itself, there are large changes in area, non-regular contours or very small edges, or where the properties of the fluid are expected to change significantly. And, from these, a structured mesh for a closed domain is built, where it is sought that the elements are as rectangular and uniform as possible, avoiding a drastic change of shape between continuous cells and maintaining a moderate aspect ratio.

This starts by defining the appropriate height for the cells in the wall by means of parameters that correspond to the models to be used. Since the flow is almost entirely axial, the *Y+* value, described in Equations 22 and 23, is quite relevant in the design of the mesh. This is the dimensionless distance from the wall in a boundary layer and gives an idea of which wall treatment or boundary condition should be used or vice versa.

$$Y+= {yu_\tau}/{v_k} \quad (22)$$

$$u_\tau = \sqrt{\frac{\tau_w}{\rho}} \quad (23)$$

In these equations (y) is the vertical distance to the wall, (u_τ) the friction velocity, (v_k) the kinematic viscosity, and (τ_w) the wall shear stress. Therefore, the value is dependent on the velocity perpendicular to the wall and varies for each cell. With this in mind, the value should be kept in an appropriate range for each method to be used and aim for most of the cells to be within that range, especially those where higher velocity or turbulent phenomena are experienced, such as the nozzle-tip, throat, and diffuser.

This limits the height of the cells in the wall for each turbulence model, and from this the vertical divisions are generated with a smoothed transition, meaning that the height of each element is slightly increased as the cells become less relevant, for example at the secondary inlet or towards the axisymmetric boundary, in order to reduce the total number of elements.

In the horizontal direction, the length of the elements in the inclined segment of the nozzle-tip is defined, and from these the adjacent elements are generated in a manner that avoids jumps in the size of the cell. Longitudinal growth factors are also applied to these elements in the areas where the properties vary little and their criticality is low, however, the aspect ratio (*Width/High*) is limited to preserve a good mesh quality.

To conclude the creation of the mesh, the boundaries are assigned as they correspond to the inputs, the output, the central axis, and the walls. In Fig. 22, the mesh developed for the k-ε model with the geometry of 0 nxp, which has a total of 33220 elements, can be seen as an example. In

addition, the shape and size of the elements, the smooth transition between them and the way the boundaries are assigned can be appreciated in detail.

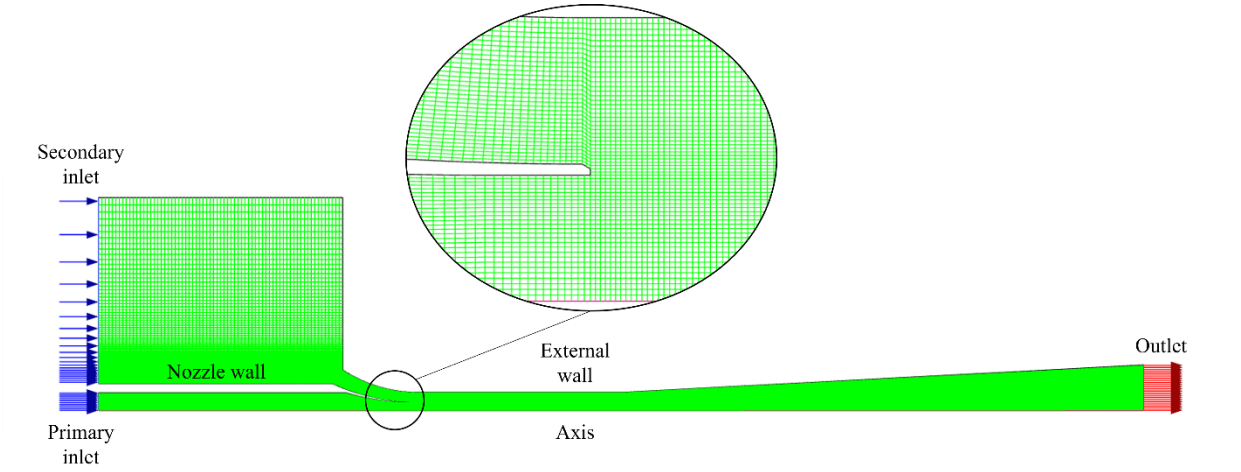

Fig. 22. Overview of the 0 nxp mesh for *k-ε* simulations – 33220 cells.

With this same approach, the meshes are created for the different nxp's and for both models. It should be noted that since the *k-ω SST* model does not use wall functions, the mesh needs to be refined enough to adequately capture the behavior near the wall. Therefore, the number of elements in it is significantly larger.

To ensure that the *k-ε* simulations are mesh independent, a mesh sensitivity analysis is performed for the nxp of 0, as the other geometries only add a region to the mesh. In this, three meshes are taken, such that each one has a greater number of elements than the previous one, the simulation is performed, and it is observed if the properties tend to converge or if they vary significantly among them. On the other hand, for *k-ω SST*, due to the high computational cost, it is reserved to the comparison between the numerical results and the universal boundary layer velocity profile, as is presented in Chapter V, and since the data is consistent, it is determined that it adequately represents the object of study.

The meshes chosen for the sensitivity analysis are 16749 elements (≈16k mesh), 33220 (≈32k mesh) and 54226 (≈54k mesh). Velocity fields are compared at 3 cross-sections, corresponding to the middle of the throat, the beginning of the diffuser and the middle of the diffuser; and the normalized total pressure at the three cross-sections where such readings were

taken in the Sanger experiments, namely 2.6, 4.8 and 10.4 D_t from the beginning of the throat. The results can be seen in Fig. 23 and Fig. 24, there the convergence in the velocity profiles is difficult to appreciate graphically, although it exists numerically, however, the third total pressure profile clearly shows the convergence. This data allows concluding that the 32k elements grid is good enough to capture the behavior of the pump, since a higher refinement would produce very similar results. It is worth mentioning that there is no variation in the residuals either.

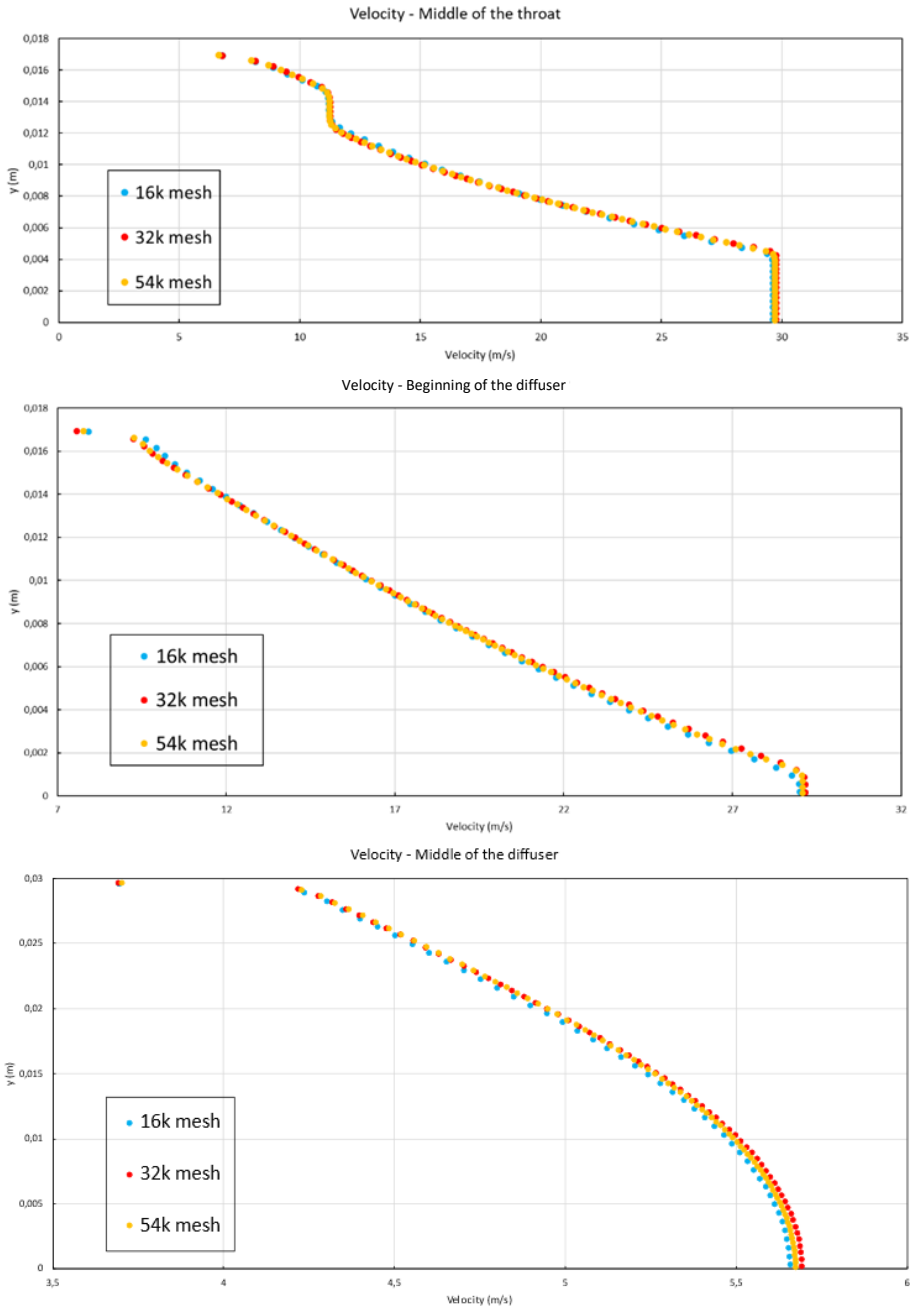

Fig. 23. Mesh sensitivity analysis – Velocity profiles.

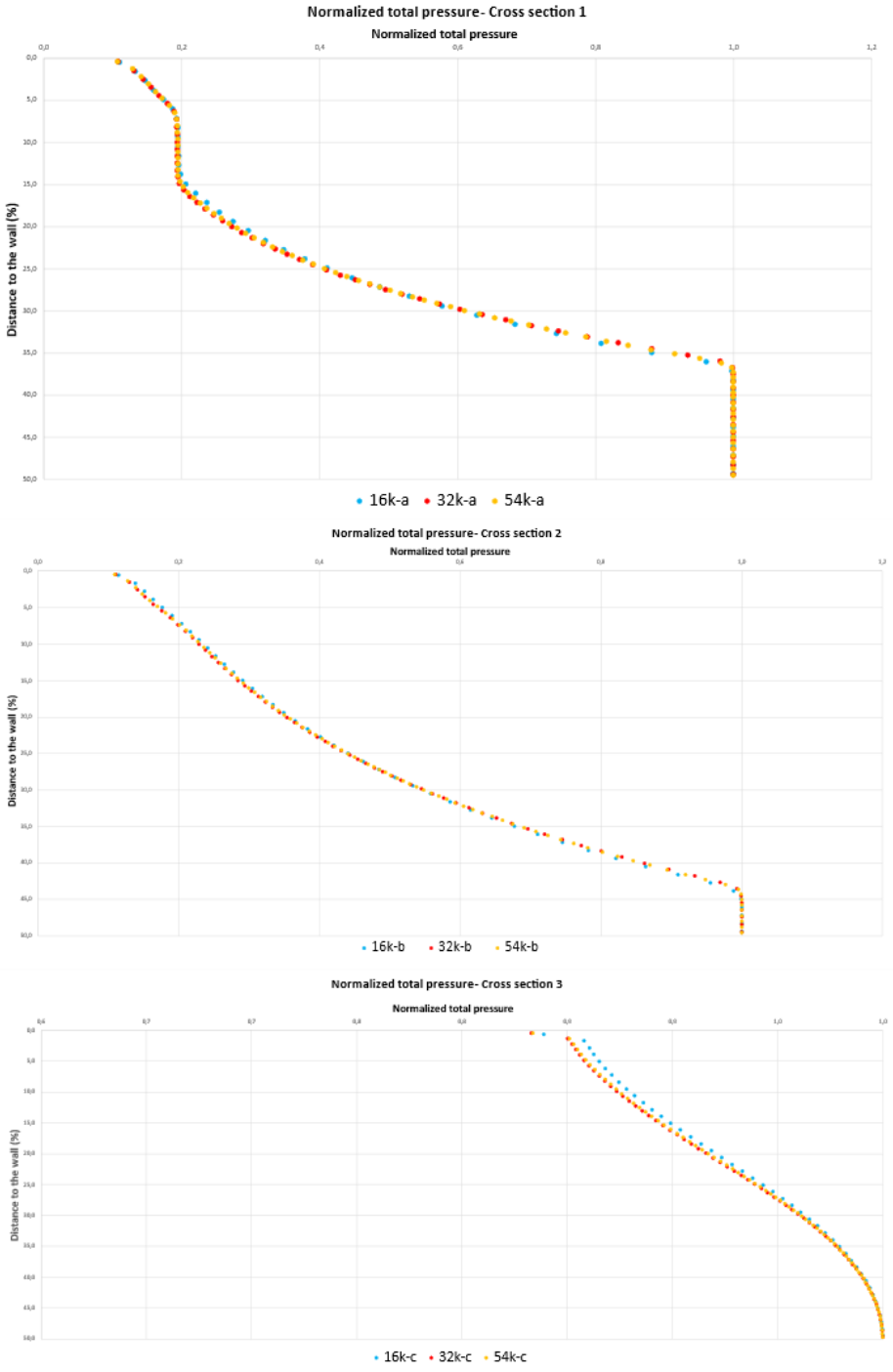

Fig. 24. Mesh sensitivity analysis – Normalized total pressure profiles.

Hence, the meshes chosen for the first simulations are 33320 elements for the nxp of 0, 38208 for the nxp of 1.36 and 41700 elements for the nxp of 2.66. In the case of *k-ω SST*, the number of cells is 900220, with a height in the wall cell on the order of $2 * 10^{-6}$ meters, which allows the domain to be adequately represented.

The quality of these meshes is analyzed by means of the "Mesh metrics" incorporated in the ANSYS software, particularly the aspect ratio, orthogonal quality, and skewness. The element quality parameter is not considered relevant for this case, as it gives an idea of how squared the cells are, however, as the flow is quasi-one-dimensional, the aspect ratio is controlled according to the relevance of the cells in the mesh, and therefore more importance is given to the aspect ratio than to this parameter.

Regarding these metrics, the Aspect Ratio should be low, especially for the cells where the flow will undergo accelerated property changes, and in the case of the other two parameters, a Skewness close to 0 and an Orthogoal Quality close to 1 are intended. These aspects, which are adjusted as the mesh is being created, are reviewed at the end of the process and it is concluded that the quality of each one of them is adequate for the simulations to be conducted.

Fig. 25 and Fig. 26 show, as an example, the metrics of the meshes without nozzle-to-throat spacing of 32k and 900k elements. It can be seen that both present very good ratios for the skewness and orthogonal quality parameters, which is to be expected since the mesh is highly structured. As for the aspect ratio, it is noted that it is mainly low, since the cells with higher values correspond to those in the secondary inlet and the duct prior to the primary nozzle, where the fluid properties are almost constant and therefore the simulation results are not affected.

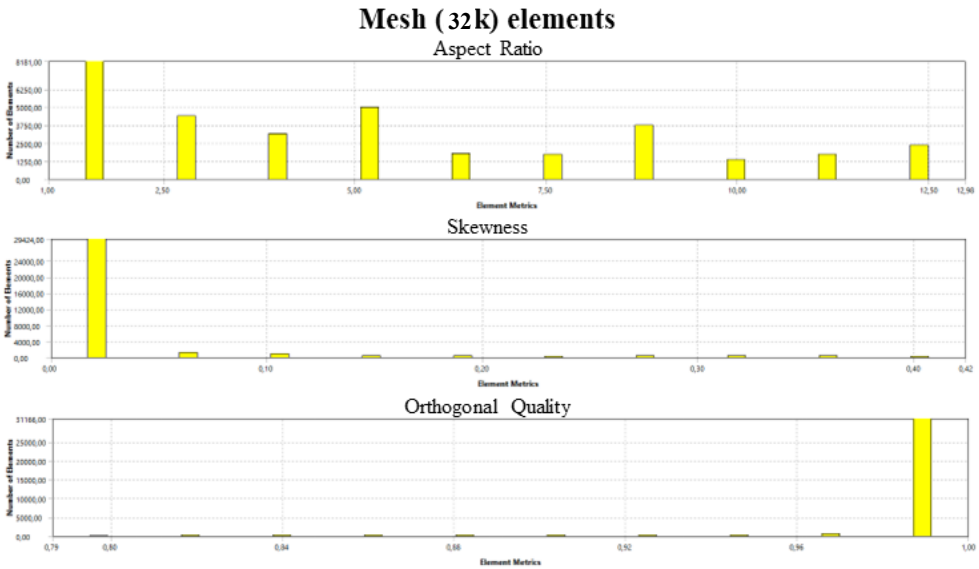

Fig. 25. Mesh metrics analysis – 32k elements mesh.

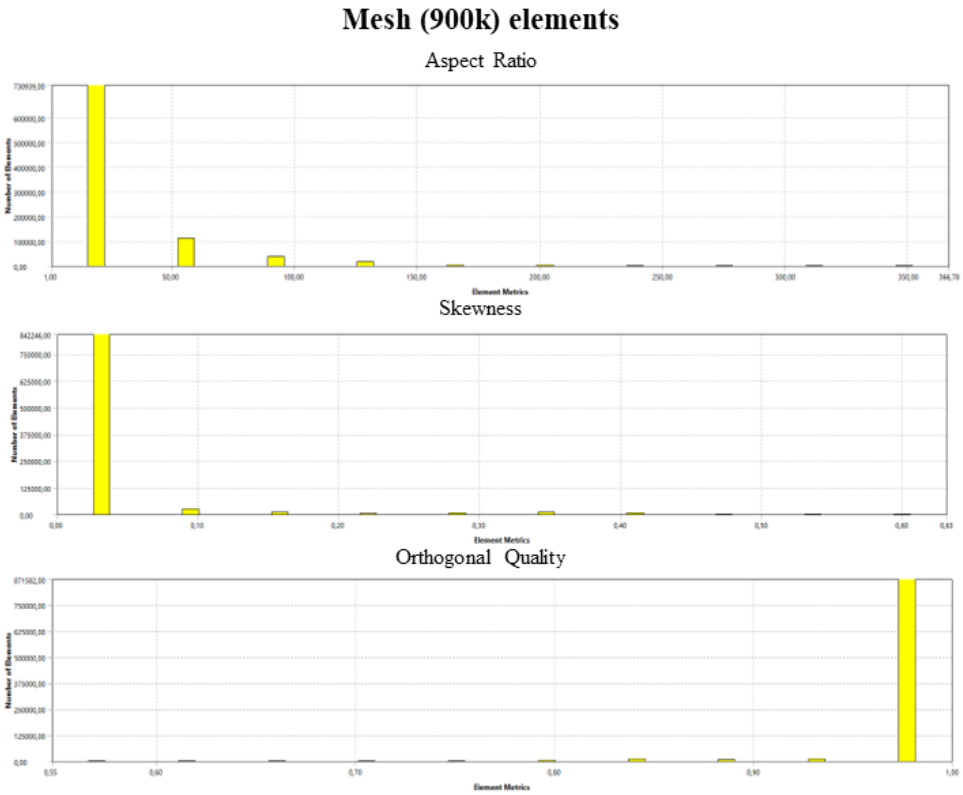

Fig. 26. Mesh metrics analysis – 900k elements mesh.

Finally, the *Y+* parameter is similarly checked in the different meshes, and it is verified that, for the most important zones, it is within the ideal ranges. Usually, *Y+* should be between 30 and 300 for *k-ε* models, and around 1 for *k-ω SST*.

In Fig. 27 and Fig. 28, the values on the top wall and the wall of the nozzle can be seen, for the 0 nxp meshes of 32k and 900k elements. In these, the relevant segment is the one after the 0.3 mark on the horizontal axis, since it corresponds to the beginning of the throat and therefore the phenomena of interest, and it is evident that it meets the condition. The zones between 0 and 0.3 can present very low or high values of *Y+* without relevance for the simulation, either because the local velocity is very low or because the cell is inclined with respect to the flow, in any case, they do not present physical implications and therefore it can be concluded that for this other aspect the developed meshes are appropriate for the simulation. More detail on this behavior is explained in the following chapter.

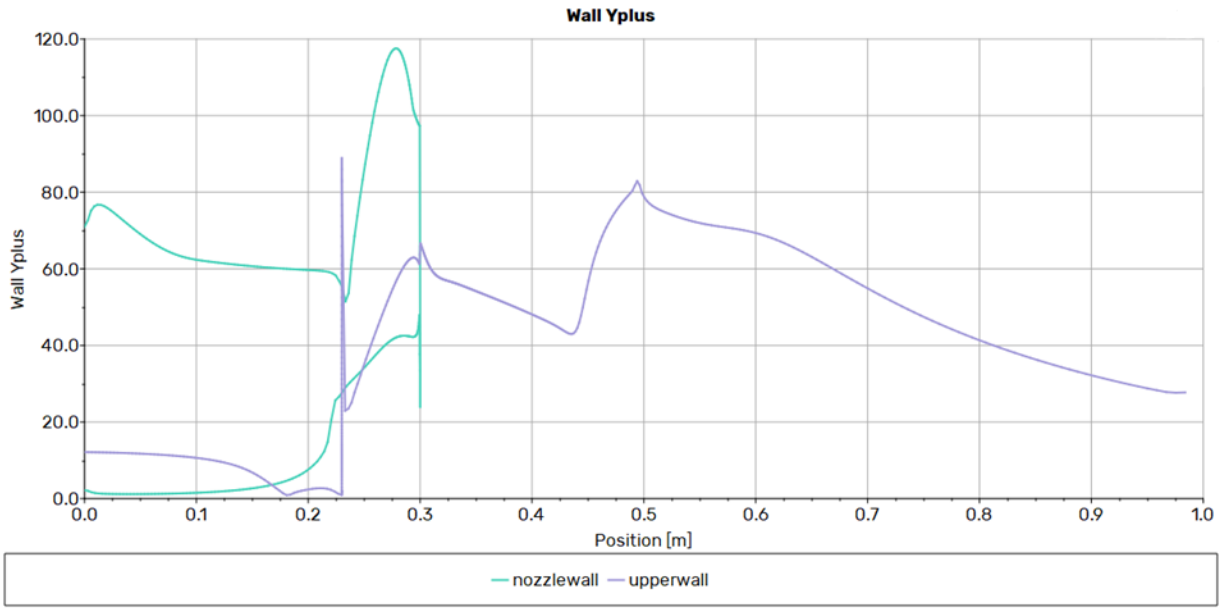

Fig. 27. Mesh *Y*+ analysis – 32k elements mesh.

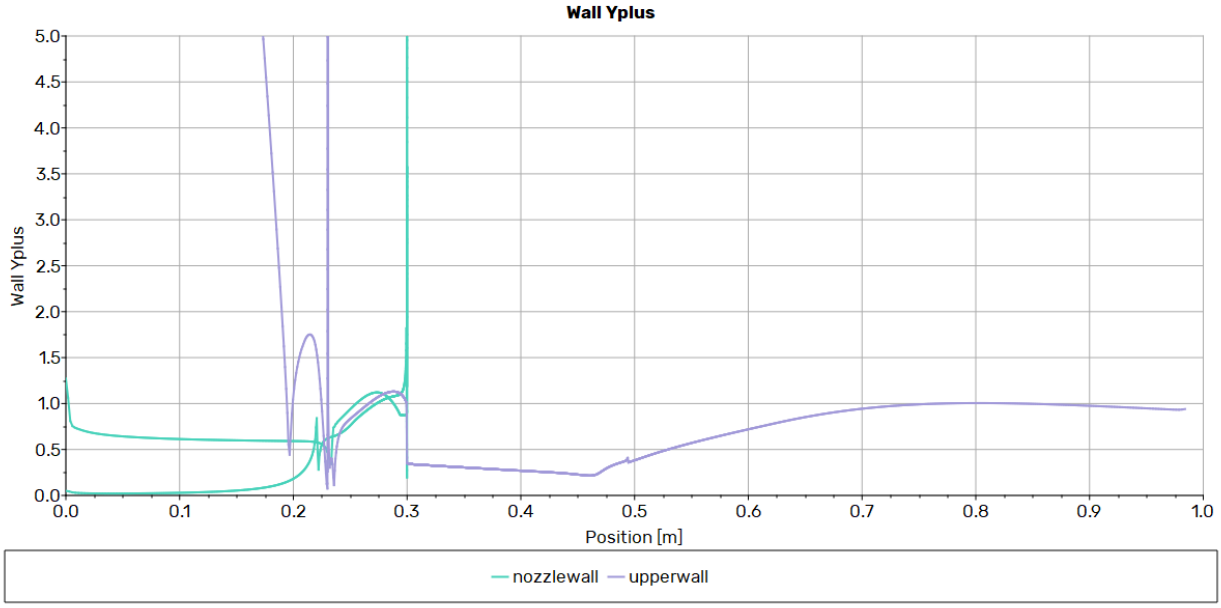

Fig. 28. Mesh *Y*+ analysis – 900k elements mesh.

D. Simulation configurations

Once the mesh is loaded in Fluent®, the simulation aspects are configured. As for the solver, a pressure-based formulation is used, with absolute velocity and in a steady and axisymmetric configuration. Gravity is disregarded for this case, since its influence is considered minimal, which is verified through results comparison. The fluid is water as it appears by default in the Fluent Database, with an operating pressure of 0 Pascals, so that the values are absolute.

As for the viscous models, standard k-ε is used with constants of 1.9 for C2, 1 for the TKE Prandtl Number and 1.2 for the TDR Prandtl Number. The near-wall treatments are standard, scalable, and enhanced wall treatment functions. Moreover, for k-ω SST the predetermined constants in the software are used.

The boundary conditions are set as can be seen in TABLE I, these follow the values indicated by Sanger and force the desired operating characteristics, meaning that the desired flow ratio is obtained by assigning to the output a value such that $\dot{m}_{out} = FR * \dot{m}_1$, while the secondary input is a constant value.

TABLE I
BOUNDARY CONDITIONS

Boundary	Condition	Value
Axis	Axisymmetric	-
Interior	Interior	-
Nozzle wall	No slip wall – Standard roughness	-
External wall	No slip wall – Standard roughness	-
Primary inlet	Mass flow inlet	3.9728 kg/s
Secondary inlet	Pressure inlet	103000 Pa
Outlet	Mass flow outlet	Calculated

Note: Boundary conditions for the simulations.

For the solution methods, the configurations presented in TABLE II are used, and for the pseudo time under - relaxation factors of the solution controls, the default values of the software are employed.

TABLE II
SOLUTION METHODS

Feature	Type
Scheme	SIMPLE
Flux type	Rhie-Chow (distance-based)
Gradient	Least Squares Cell Based
Pressure	Second Order
Momentum	Second Order Upwind
Turbulence Kinetic Energy	First Order Upwind
Turbulence Dissipation Rate	First Order Upwind

Note: Solution methods for the simulations.

The convergence criterion for all residuals is set to 1e-08¸ although the pressure fields, velocity, system efficiency and other properties are checked for their convergence. And finally, a standard initialization is performed, meaning that the cell properties are filled with constant values, which are computed from the primary inlet, to then assign an initial number of iterations, run the simulation and, depending on the convergence, add iterations if necessary.

This concludes the computational setup that deals with the whole process from the creation of the geometry to the configuration of the simulations in the software. Which leads to Chapter V, where the results of the multiple simulations are analyzed, the behavior of the device is observed, and the results are compared between the different methods and with the experimental data from the validation source.

V. ANALYSIS AND RESULTS

Firstly, the results of the simulations with the k-ε method are analyzed, comparing the different wall-functions for the three nozzle-to-throat spacings and the behavior at different FR. In all cases the simulations converged correctly, this is verified by checking the residuals, most of which reach the convergence criterion, and for the other ones, they present an oscillatory behavior maintained around 1e-07.

Complementarily, the convergence in the values of efficiency, velocity, and pressure in a cross-section in the middle of the throat is analyzed. These values tend to stabilize as the solution is developed and thus show the proper convergence of the simulations. As an example, since all simulations behave similarly, the convergence graphs of these values are presented in Fig. 29, Fig. 30, and Fig. 31, for the mesh without throat spacing and standard wall function, showing how the values tend to be constant as the iterations progress.

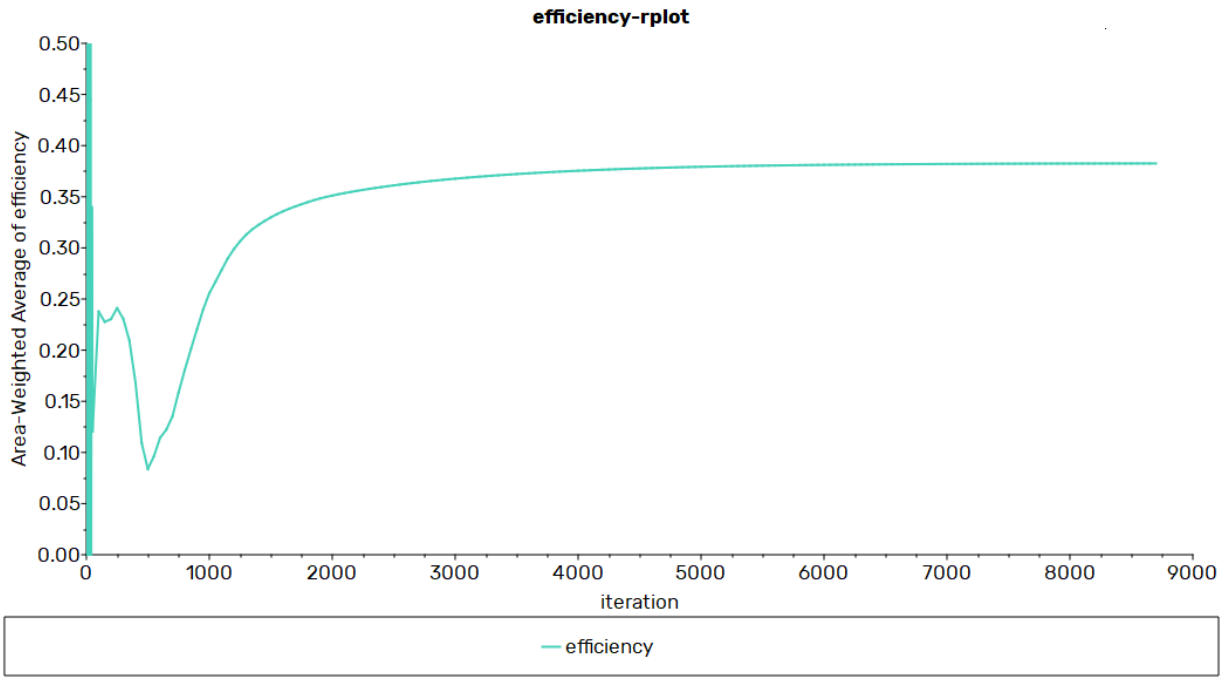

Fig. 29. Convergence of the efficiency – 0 nxp standard wall function.

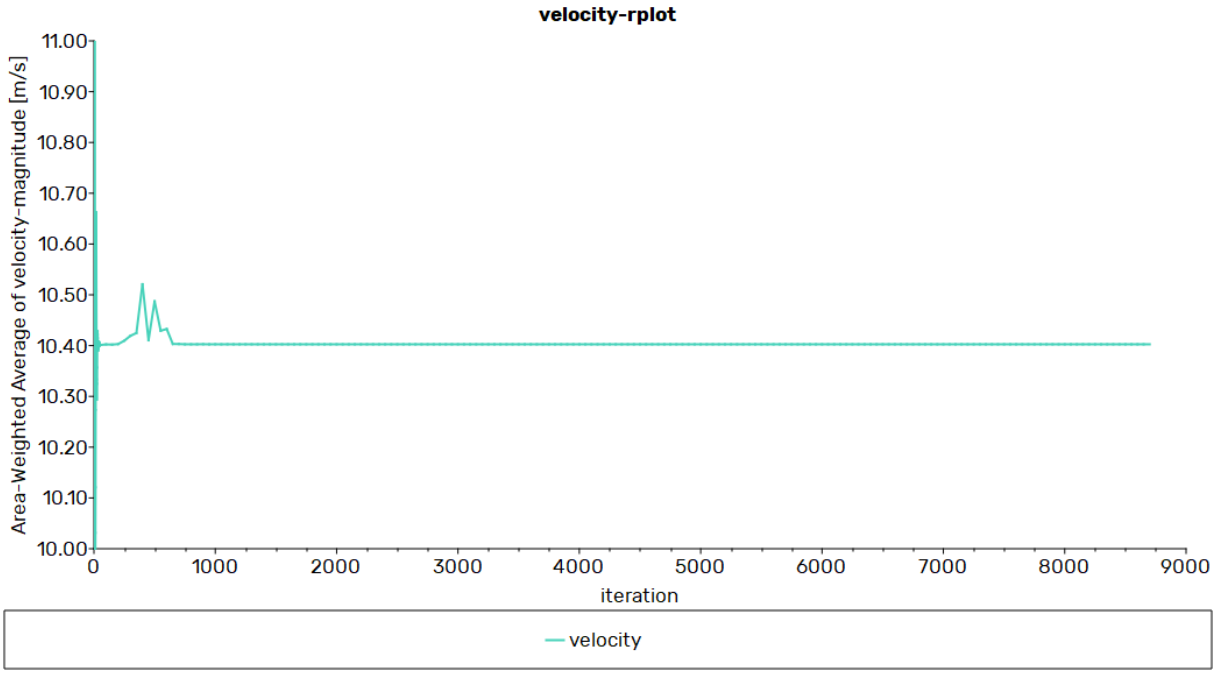

Fig. 30. Convergence of velocity – middle of the throat – 0 nxp standard wall function.

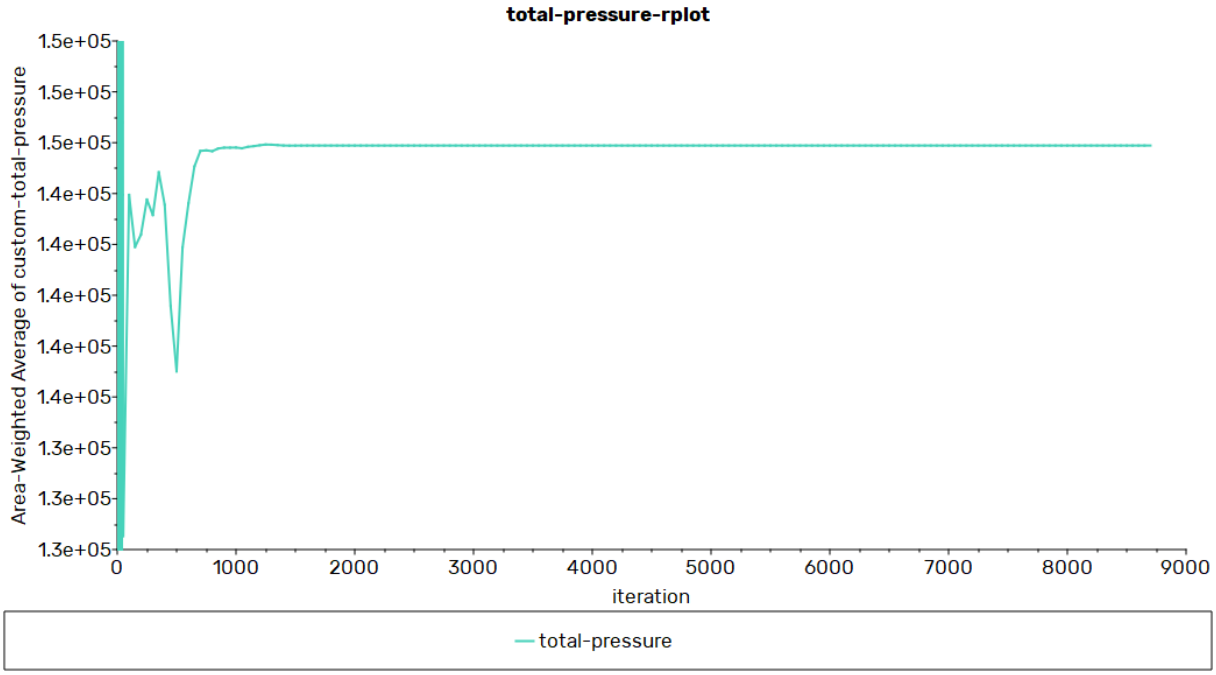

Fig. 31. Convergence of total pressure – middle of the throat – 0 nxp standard wall function.

To establish which wall function matches the results better, the three types (standard, scalable and enhanced wall treatment) are simulated for the meshes with 0, 1.36 and 2.66 D_t spacing, for the different flow ratios that can be compared with the experimental results of Sanger. Comparative efficiency plots between these cases and the validation source data are presented in Fig. 32, Fig. 33, and Fig. 34.

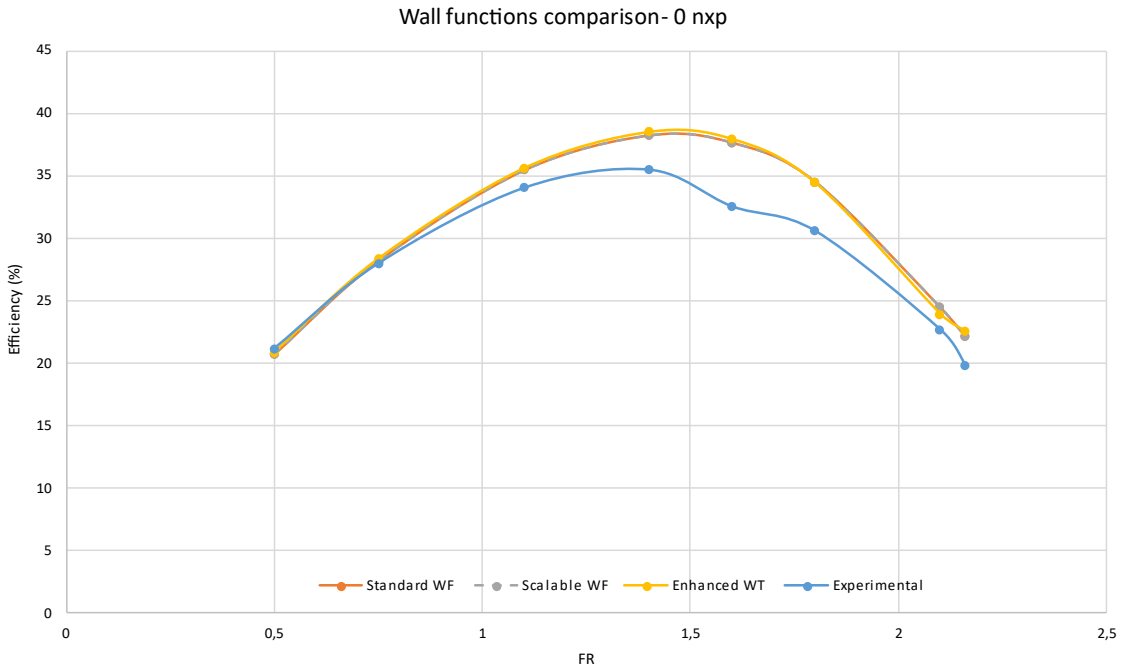

Fig. 32. Wall functions comparison – 0 nxp.

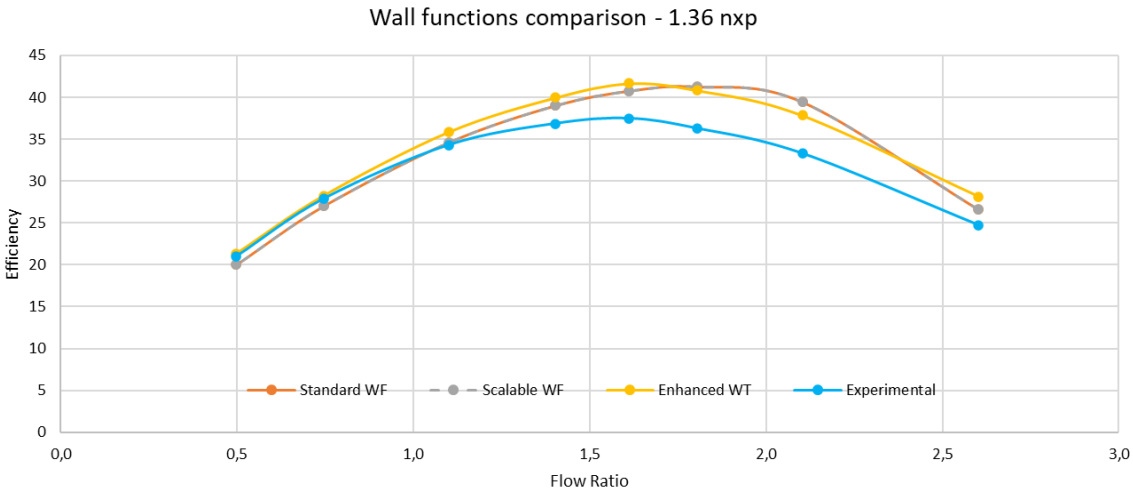

Fig. 33. Wall functions comparison – 1.36 nxp.

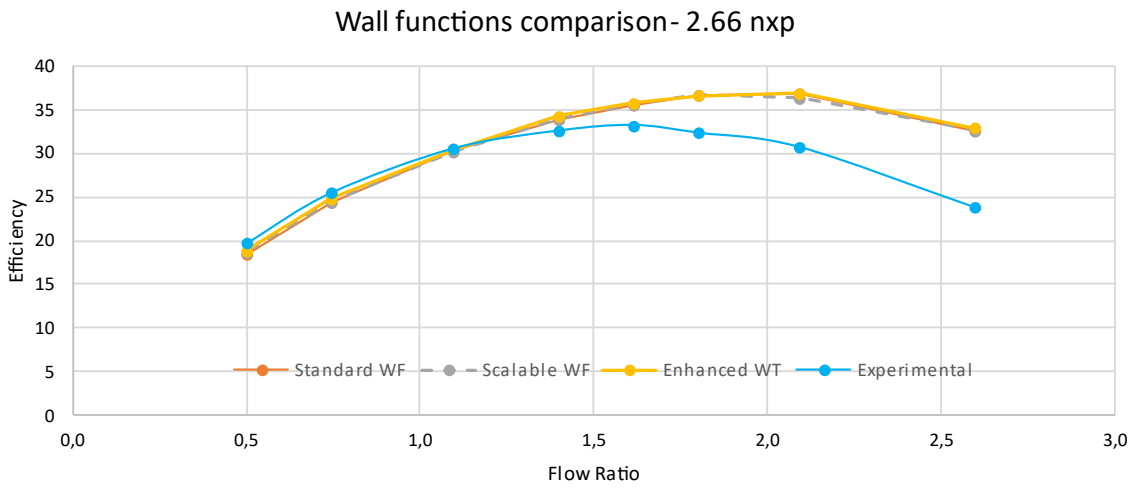

Fig. 34. Wall functions comparison – 2.66 nxp.

In addition to the general efficiency comparison, in order to evaluate the accuracy of these simulations, they are compared with the information available from the validation source. This is the pressure coefficient C_p at flow ratios of 1.4 and 1.6, and the total pressure in the three cross sections, at 2.6, 4.8 and 10.4 D_t from the start of the throat for a nxp of 0 and a FR of 1.6, as shown in Fig. 35 - Fig. 39.

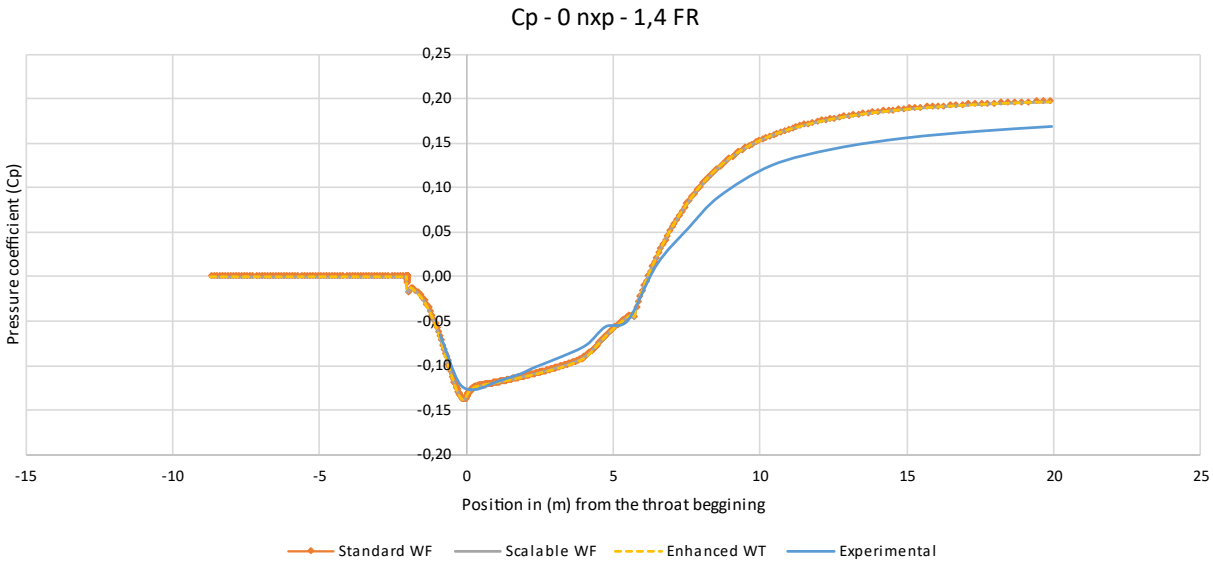

Fig. 35. Wall functions comparison – Pressure coefficient – 0 nxp 1.4 FR.

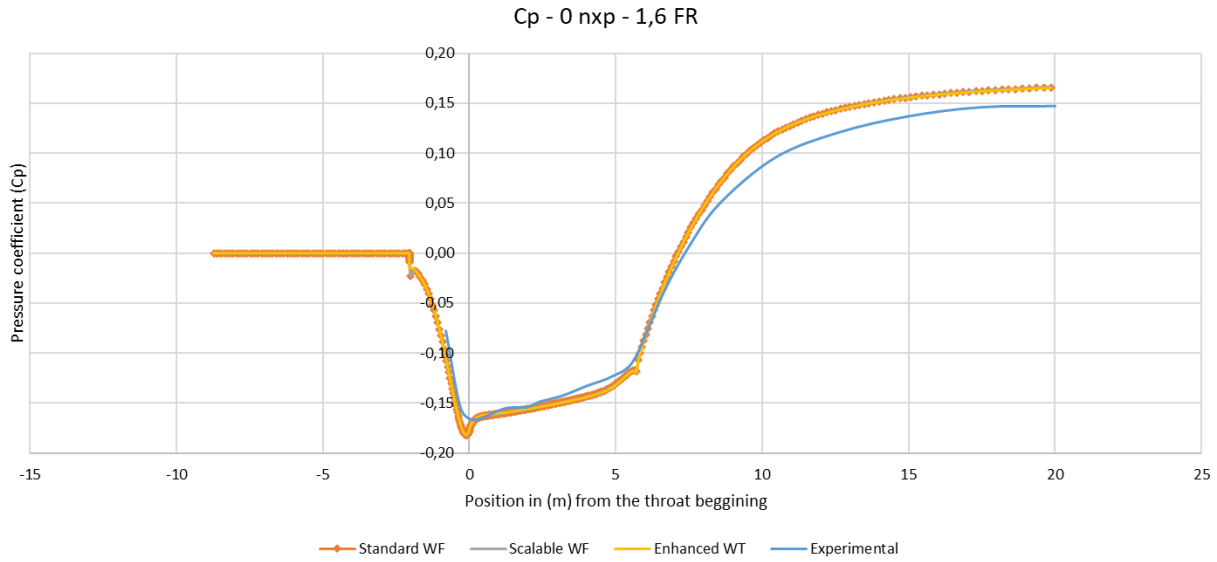

Fig. 36. Wall functions comparison – Pressure coefficient – 0 nxp 1.6 FR.

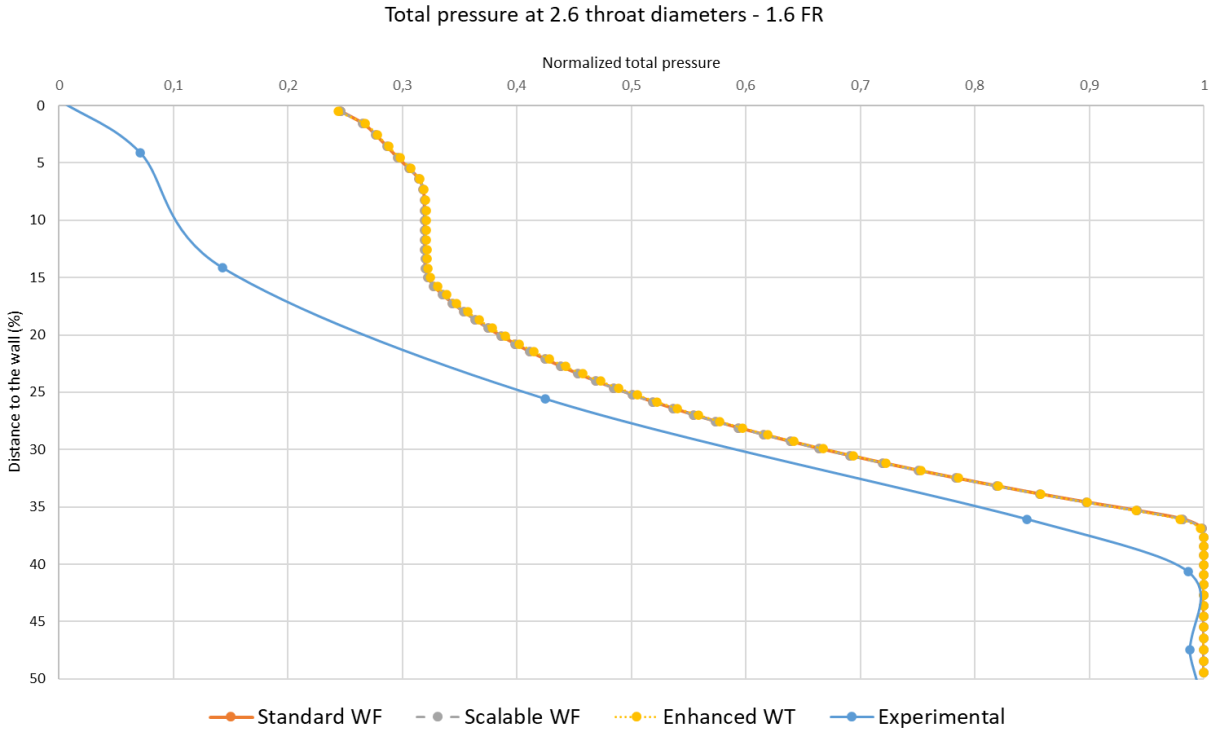

Fig. 37. Wall functions comparison – Total pressure at 2.6 D_t – 0 nxp 1.6 FR.

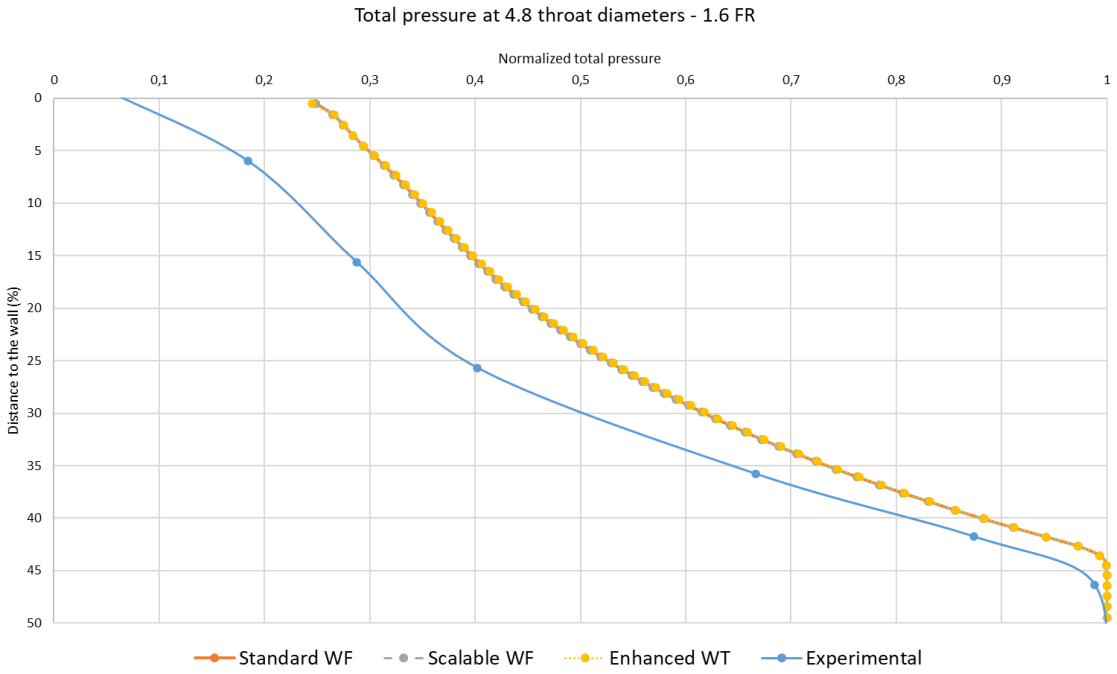

Fig. 38. Wall functions comparison – Total pressure at 4.8 D_t – 0 nxp 1.6 FR.

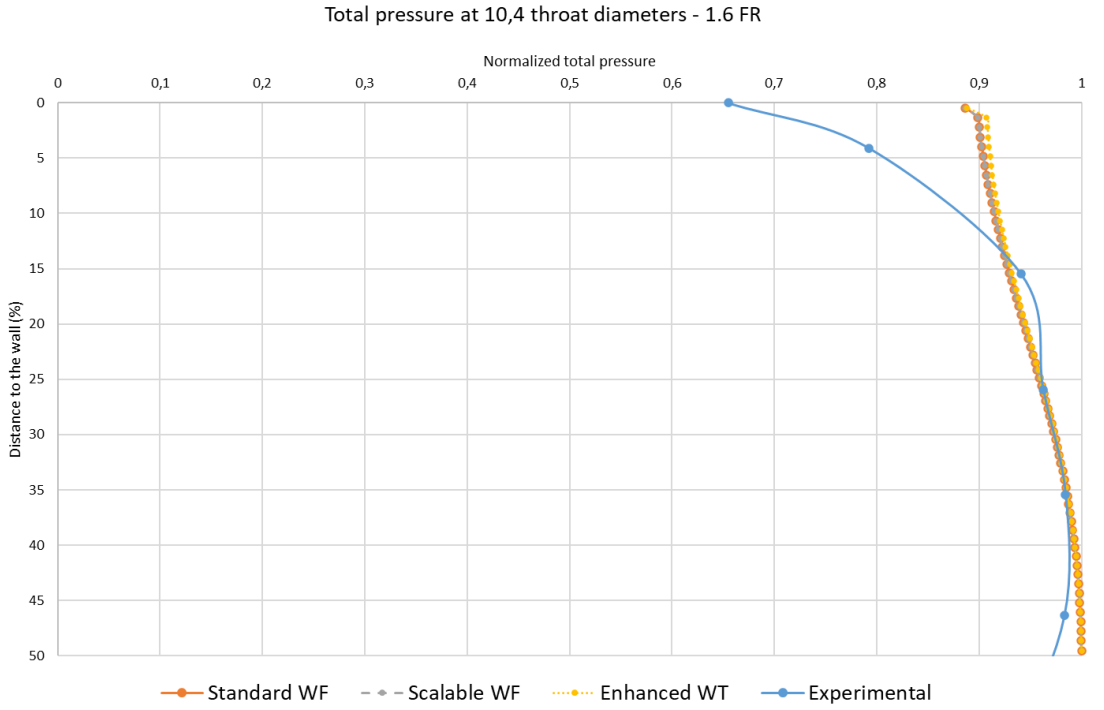

Fig. 39. Wall functions comparison – Total pressure at 10.4 D_t – 0 nxp 1.6 FR.

The results indicate that the different wall functions yield similar results, especially for the pressure coefficient and total pressure, but when calculating the average relative error for efficiency, it is found that the standard wall function is the one that most accurately captures the behavior of the jet-pump, with an average relative error of 7.3%, in contrast to the 7.32% of the scalable wall function and the 8.32% of the enhanced wall treatment.

Regarding the velocity and static pressure contours, these allow identifying the mixing zone visually and understanding the behavior of the device. Other alternatives to these are the turbulent kinetic energy, or transverse profiles of these fields along the jet-pump, however, since they are all similar, the velocity and static pressure contours of the different geometries at different FR are presented below in Fig. 40 - Fig. 45.

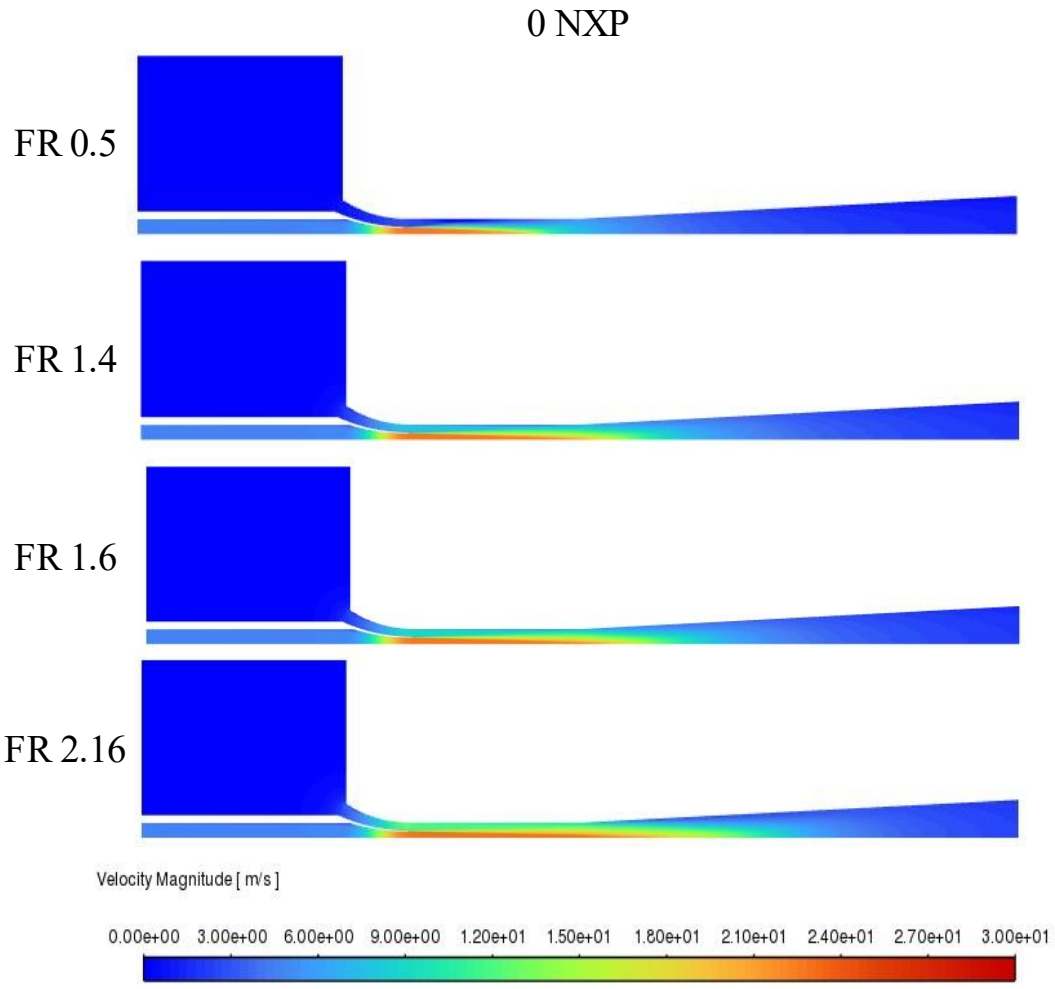

Fig. 40. Velocity contours for different FR – 0 nxp.

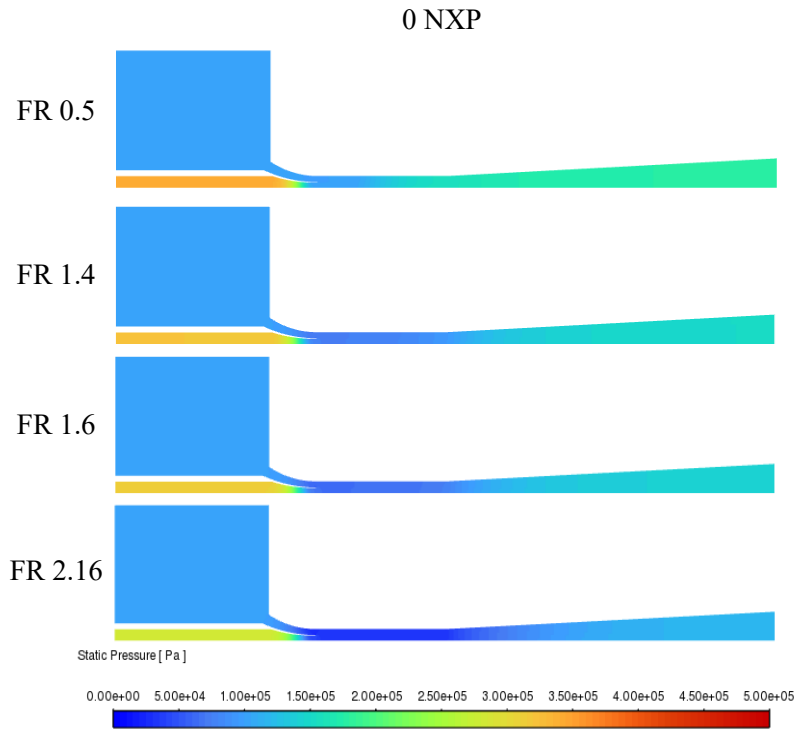

Fig. 41. Static pressure contours for different FR – 0 nxp.

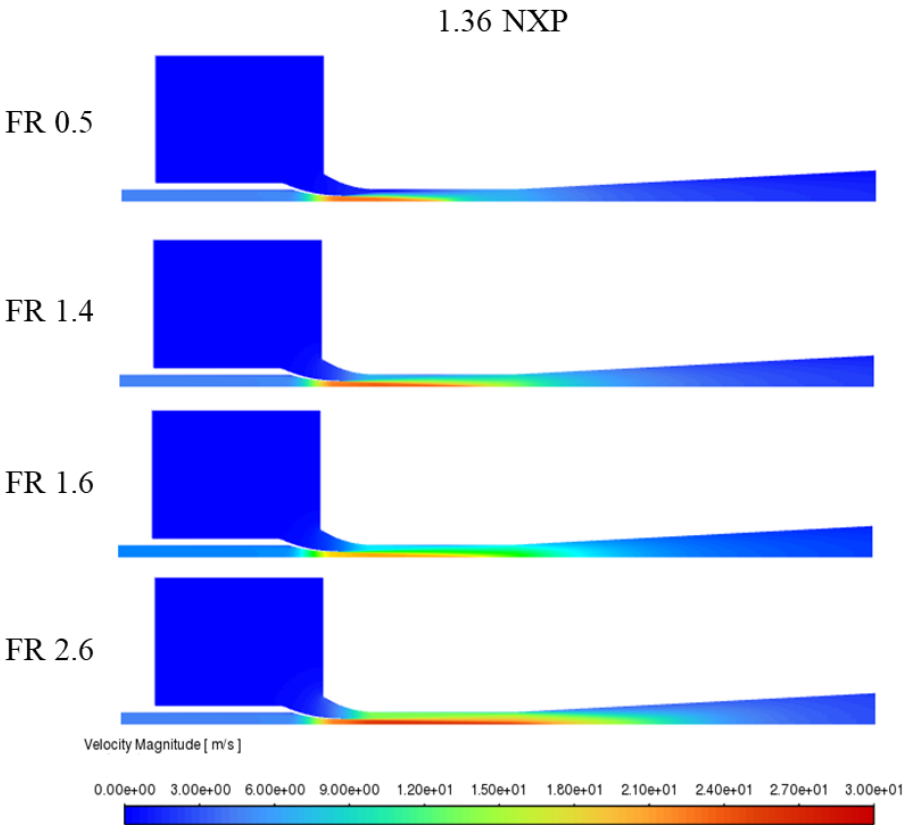

Fig. 42. Velocity contours for different FR – 1.36 nxp.

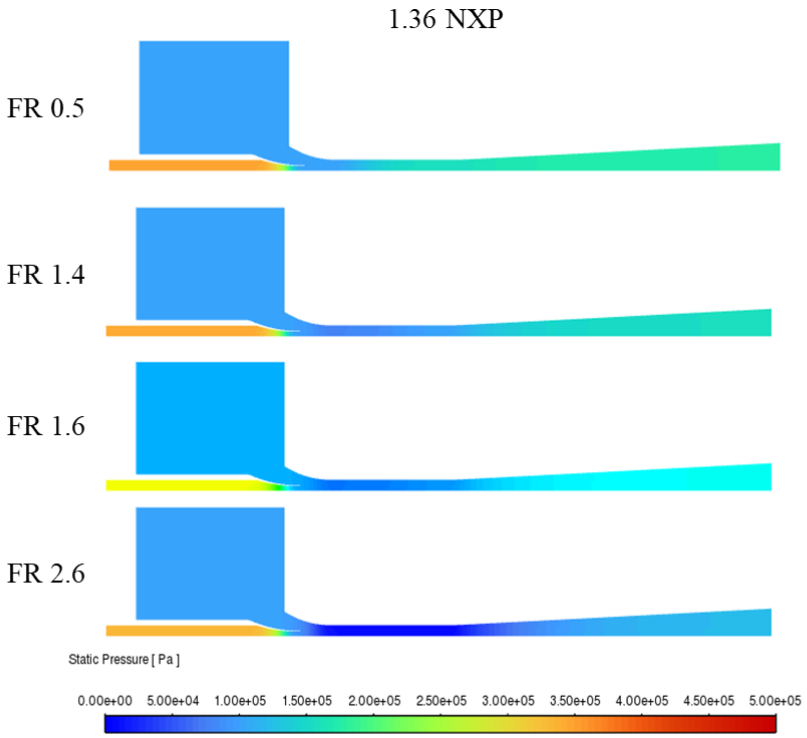

Fig. 43. Static pressure contours for different FR – 1.36 nxp.

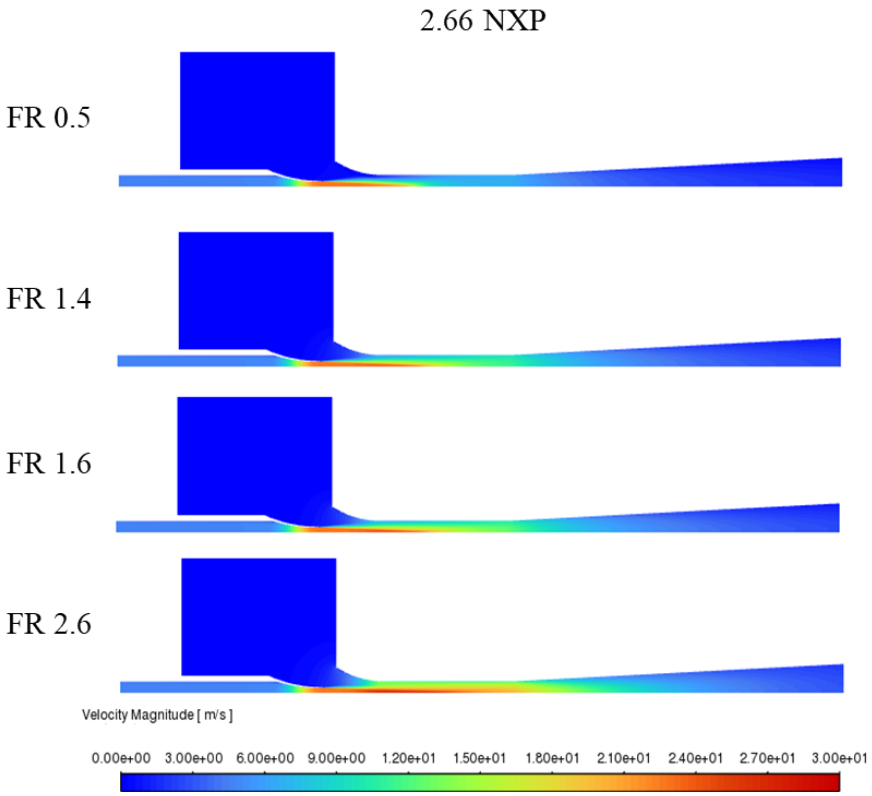

Fig. 44. Velocity contours for different FR – 2.66 nxp.

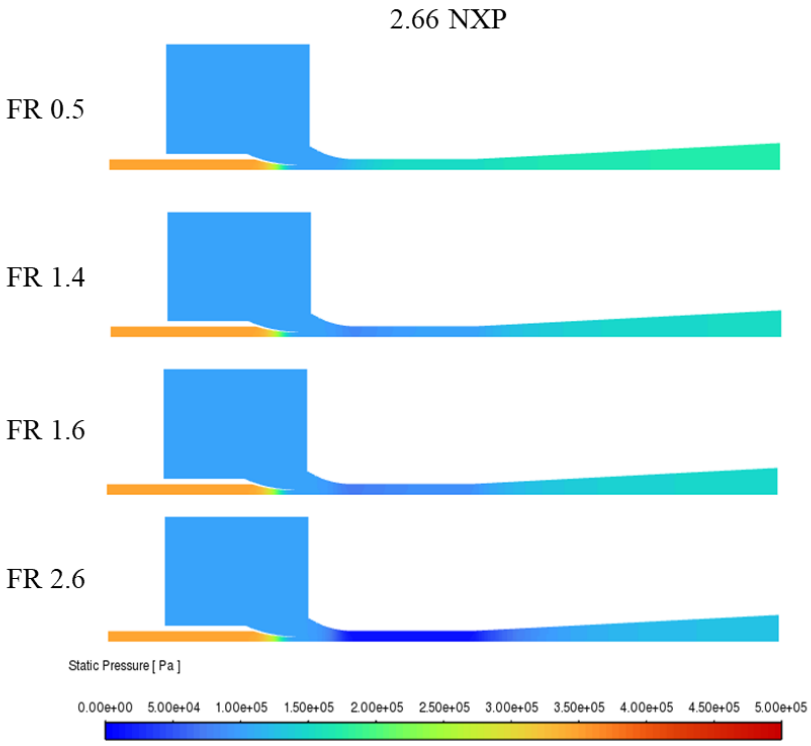

Fig. 45. Static pressure contours for different FR – 2.66 nxp.

For the simulations under k-ω SST, it is verified that the simulation converges adequately, apart from the residuals, as they properly reach the criterion; and that the behavior in the near-wall regions is being accurately captured for the 900k element mesh. For this, the convergence of the efficiency is analyzed, and the theoretical boundary layer is compared, finding that there is a good relationship between the empirical and numerical data, as shown in Fig. 46 and Fig. 47.

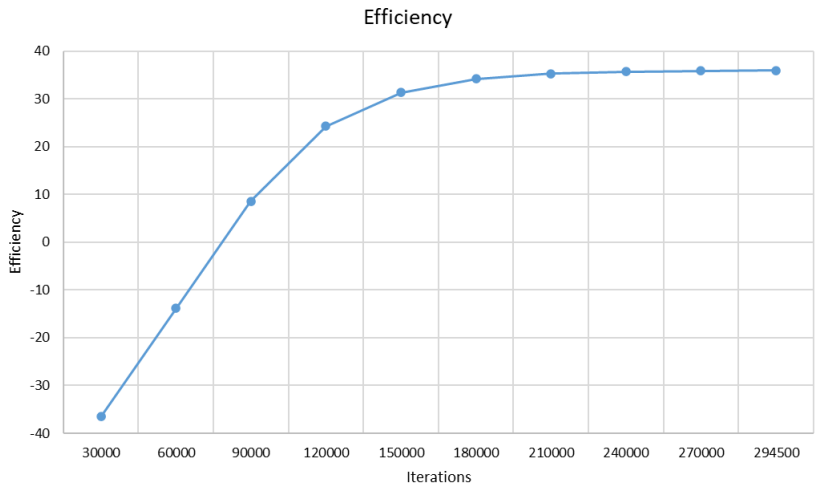

Fig. 46. Efficiency convergence for the 900k mesh.

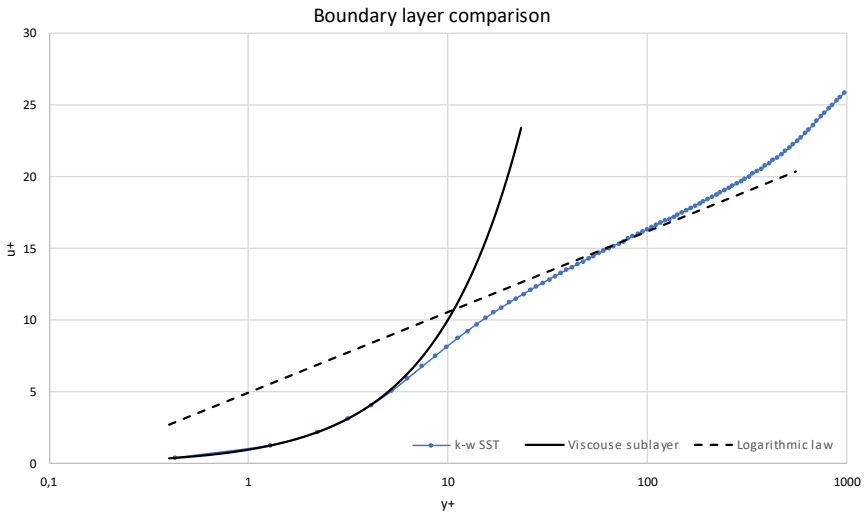

Fig. 47. Boundary layer comparison for the 900k mesh.

Regarding Y+, the radial velocity contour in Fig. 48, meaning in direction from the central axis towards the wall, shows how the cells on the vertical wall and the inclined plane of the nozzle-tip experience very different velocities. The lower cells, as a consequence of the inertia of the primary jet, experience almost zero perpendicular velocity, while those at the upper edge, as the fluid is entrained towards the throat, experience higher values. Considering that Y+ is a function of the perpendicular velocity to the cell, the variability observed in Fig. 27 and Fig. 28 is explained. Furthermore, this behavior, where the mixing occurs at a certain distance from the nozzle, justifies why these cells are not so relevant in terms of this parameter and the reason for giving priority to those found in the throat wall and the diffuser.

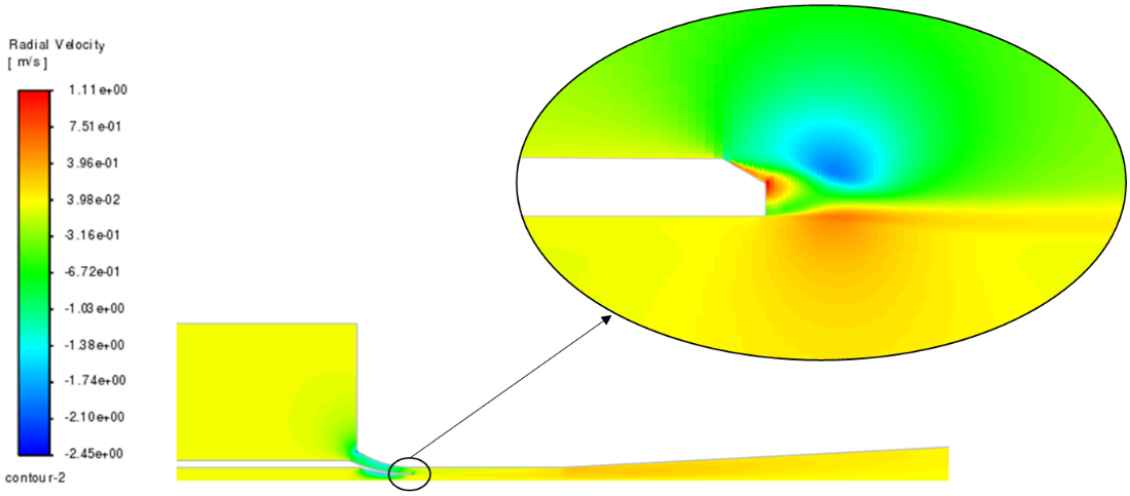

Fig. 48. Radial velocity contour for the 900k mesh.

Subsequently, the results of the pressure coefficient and total pressure are plotted under the same existing conditions for *k-ε*, and compared with the previous results of the standard wall function simulations and the validation data, as depicted in Fig. 49 - Fig. 53. From these data, it is calculated that the average relative error in C_p for the *k-ε* model is 10.68%, while for the second model is 3.21%.

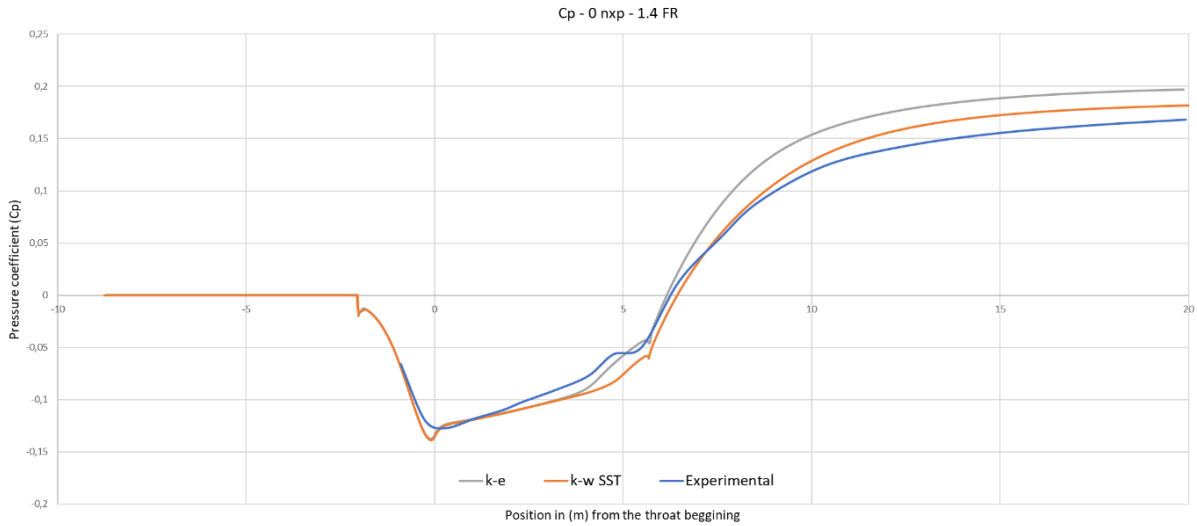

Fig. 49. Pressure coefficient – 0 nxp 1.4 FR.

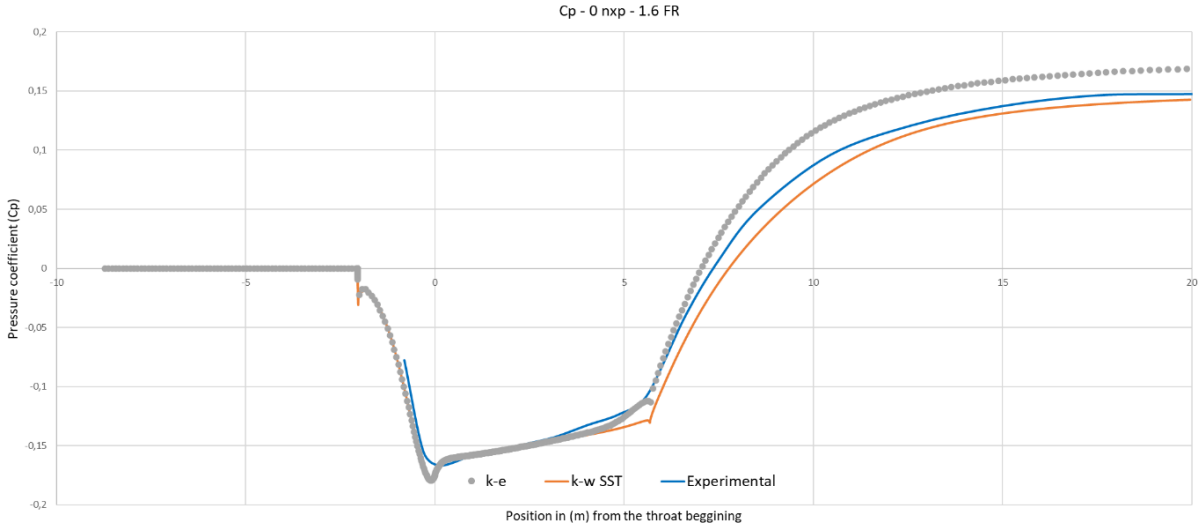

Fig. 50. Pressure coefficient – 0 nxp 1.6 FR.

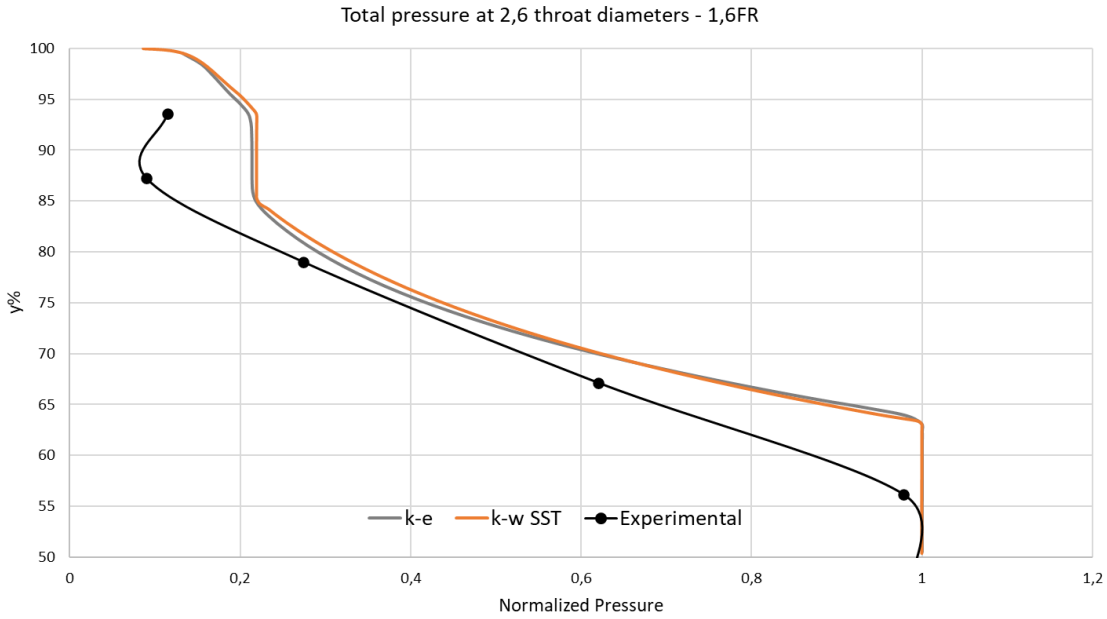

Fig. 51. Total pressure at 2.6 D_t – 0 nxp 1.6 FR.

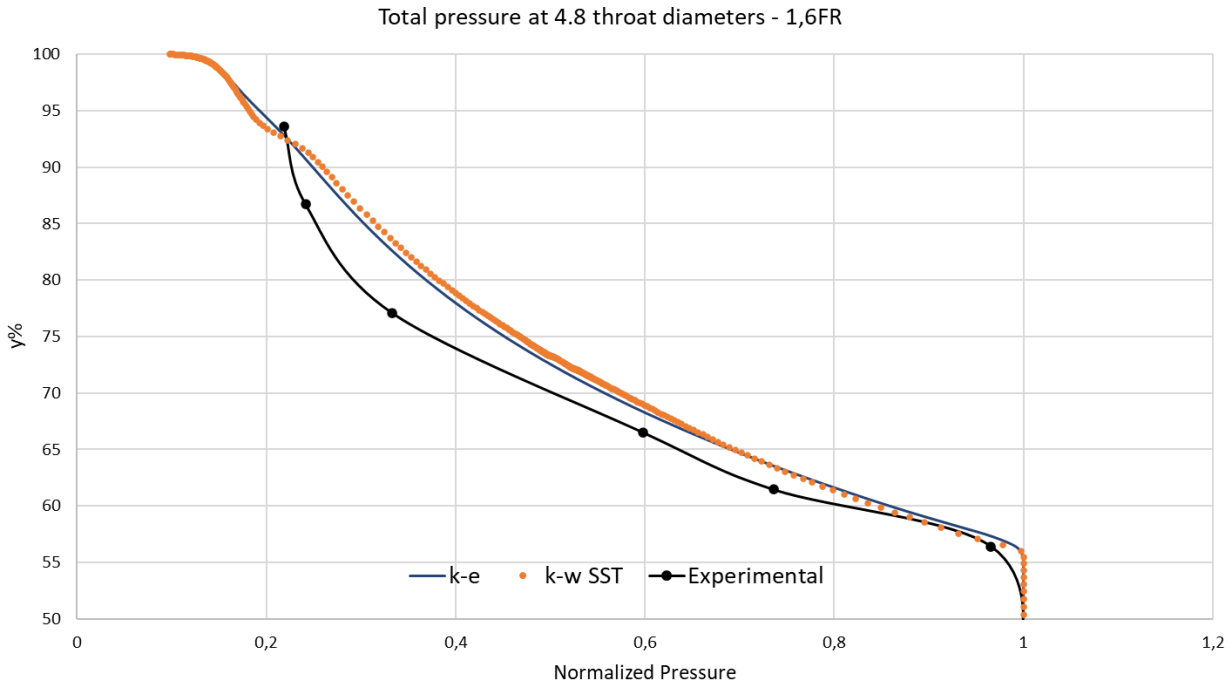

Fig. 52. Total pressure at 4.2 D_t – 0 nxp 1.6 FR.

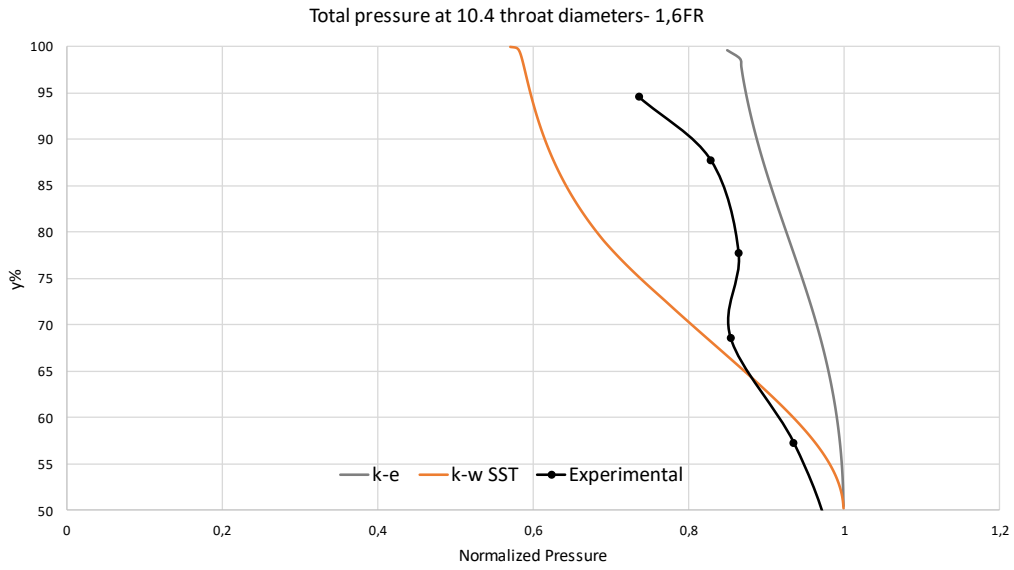

Fig. 53. Total pressure at 10.4 D_t – 0 nxp 1.6 FR.

Finally, Fig. 54 compares the overall efficiency of the device with the Sanger results and those of the *k-ε* model with standard wall function. Although the *k-ω SST* model captures better the behavior at the points of maximum efficiency, it loses accuracy for higher flow ratios. Numerically, the *k-ε* model presents an average relative error for efficiency of 7.3%, in contrast to the 8.47% of *k-ω SST*.

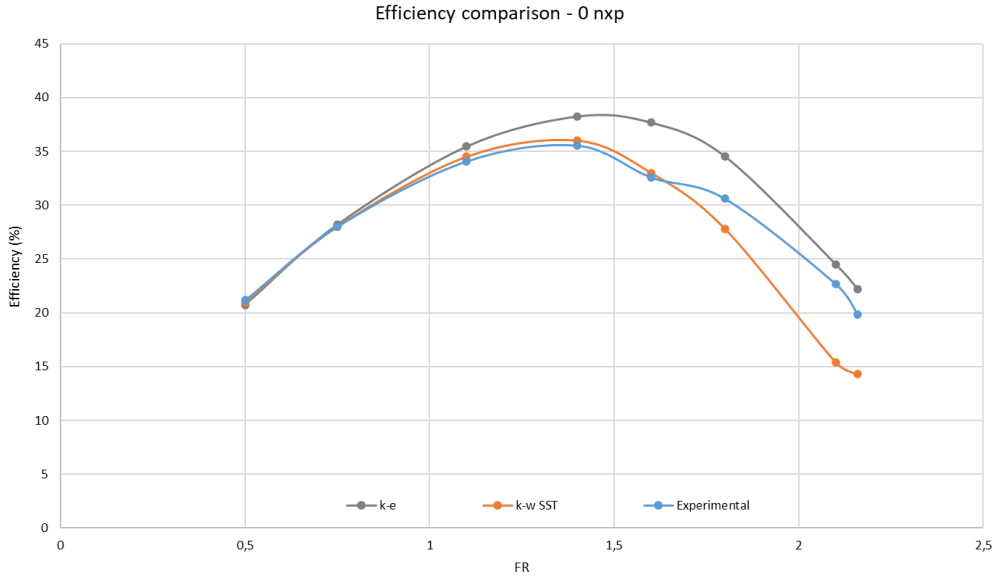

Fig. 54. Efficiency comparison between models – 0 nxp.

VI. CONCLUSIONS

The computational simulation process of the performance of a subsonic jet-pump operating with water as fluid, using RANS turbulence models, demonstrates the ability to predict with high accuracy the pressure and velocity fields, the pressure coefficient, and the overall efficiency of the device for different designs and operating conditions, such as the three different geometries and the eight flow ratios used.

The information and models supporting the validity of the simulations can be found in the reference framework. Where Sanger's tests and experimental results allow comparing the data obtained from the simulations, determining their reliability. While the work of other authors in the theoretical and experimental approaches, and especially in the numerical analysis, allows establishing the most appropriate conditions and characteristics for the simulation environment in this case of study.

A set of simplifications that facilitate the computation without considerably affecting the results, such as the axisymmetric two-dimensional representation, are included in the developed geometries, which show the same dimensions as those used by Sanger in the experimental runs. This allows using the results presented there as a comparative or validation metric for the simulations, since the device is well represented.

Furthermore, the meshes elaborated for the different models correctly represent the whole domain, allowing to adequately capture the phenomena in its entirety, including the near-wall regions. The quality of these, reflected in the mesh quality metrics, shows that the elements are highly structured and in accordance with the geometry of the problem, which translates into accuracy and reliability of the results.

Additionally, the mesh sensitivity analysis for the k-ε model, proves the independence for the 32k elements mesh and the respective ones for the other geometries. On the other hand, the agreement between the 900k elements mesh data and the theoretical boundary layer shows that the behavior of the fluid in proximity to the wall is being properly captured. This is complemented by

the results of the $Y+$ parameter, which proves to be in the appropriate ranges for most of the cells, especially those that, due to their location, are of greater relevance.

The imposed boundary conditions, namely the mass flow through the boundaries, the pressure at the secondary inlet and the wall condition, properly comply with limiting the operating behavior of the jet-pump according to the experimental setups of the validation source. While the software configurations are consistent with the specific characteristics and requirements of the case of study, ensuring the stability, convergence, and accuracy of the models.

As for the simulations, all of them converged satisfactorily, as evidenced by the residuals and the pressure, velocity, and efficiency plots with respect to the iterations. This shows that the values are well stabilized and therefore the simulation can be considered complete.

The standard wall function of the k-ε model is the one that best represents the behavior of the jet-pump, with an average relative error for efficiency of 7.3%, while the scalable wall function presents 7.32%, and the enhanced wall treatment 8.32%. The values for the pressure coefficient C_p and the total pressure at the three cross-sections are practically identical, and therefore no function can be distinguished as significantly better than the others.

The velocity contours of the k-ε simulations with standard wall function, indicate that as the flow ratio increases, the mixing location moves away from the nozzle tip, this can be seen as the zone where the primary jet's core disappears to produce a smoother cross-section. Evidencing what is presented in the reference framework, as the mixing location approaches the end of the throat, the efficiency reaches its maximum, as is the case for the flow ratios of 1.4 and 1.6, while it decreases rapidly as it continues into the diffuser due to sudden expansion losses.

In turn, the pressure contours prove that at lower flow ratios there is a higher head ratio, which means a better pumping effect in the device, or in other words, that more pressure energy is being generated relative to the kinetic energy of the input fluid. Again, showing that the jet-pump behavior is being adequately represented.

The *k-ω SST* model, also shows the capability to forecast with high accuracy the behavior of the device, particularly at the points of maximum efficiency, however, it drifts rapidly for higher flow ratios. Quantitatively, this model presents an average relative error for the efficiency of 8.47% and for the pressure coefficient C_p of 3.21%, while the values for *k-ε*, are 7.3% and 10.68% respectively.

Based on the above, it is concluded that the addressed models are capable of accurately representing the phenomena that govern the behavior of the jet-pumps, where *k-ε* better captures the internal flow field and the phenomena occurring in the diffuser, which explains the agreement of the data for the higher FRs; and *k-ω SST* better captures the near-wall behavior, as expected, and therefore the dependent parameters such as efficiency and especially the pressure coefficient are better represented.

Finally, for further work, it is suggested to:

1. Compare these results with those of LES and DNS-LES simulations, to determine the improvement of the performance prediction in consideration of the required computational resources.
2. Implement a hybrid model such that *k-ω SST* is used up to the maximum efficiency and *k-ε* thereafter.
3. Considering that the simulation environment is validated, the performance of different geometries and operational configurations of the jet-pumps can be evaluated in order to optimize a particular application, obtaining through the computational modeling a faster and more versatile design process than conventional prototyping.

REFERENCES

[1] N. L. Sanger, “An Experimental Investigation of Several Low-Area-Ratio Water Jet Pumps,” *Journal of Basic Engineering*, vol. 92, no. 1, pp. 11–19, Mar. 1970, doi: 10.1115/1.3424917.

[2] P. Zheng, B. Li, and J. Qin, “CFD simulation of two-phase ejector performance influenced by different operation conditions,” *Energy*, vol. 155, pp. 1129–1145, Jul. 2018, doi: 10.1016/j.energy.2018.04.066.

[3] N. L. Sanger, “Noncavitating performance of two low-area-ratio water jet pumps having throat lengths of 7.25 diameters | WorldCat.org.” Accessed: Jul. 17, 2023. [Online]. Available: https://www.worldcat.org/es/title/noncavitating-performance-of-two-low-area-ratio-water-jet-pumps-having-throat-lengths-of-725-diameters/oclc/219896840

[4] M. I. Stewart, *Surface Production Operations*. Elsevier, 2019. doi: 10.1016/C2009-0-20243-1.

[5] H. Li, H. Li, X. Huang, Q. Han, Y. Yuan, and B. Qi, “Numerical and Experimental Study on the Internal Flow of the Venturi Injector,” *Processes*, vol. 8, no. 1, p. 64, Jan. 2020, doi: 10.3390/pr8010064.

[6] N. L. Sanger, *Noncavitating and Cavitating Performance of Two Low-area-ratio Water Jet Pumps with Throat Lengths of 5.66 Diameters*. in NASA technical note. National Aeronautics and Space Administration, 1968. [Online]. Available: https://books.google.ca/books?id=a8E3C3mAdU8C

[7] A. Ravan Ghalati, M. O. Sandoval Pinto, S. Croquer Perez, S. Poncet, J. Lacey, and H. Nesreddine, “Numerical modelling of liquid water jet pumps,” in *ENFHT 2024 unpublished*, London, Apr. 2024.

[8] A. Ravan Ghalati, S. Croquer, H. Nesreddine, S. Poncet, and J. Lacey, “1D modelling of the liquid-gas jet pump performance,” in *Progress in Canadian Mechanical Engineering. Volume 6*, Sherbrooke, Canada: Université de Sherbrooke. Faculté de génie, May 2023. doi: 10.17118/11143/20983.

[9] J. E. Gosline and M. P. O’Brien, *The Water Jet Pump*, 3rd ed., vol. 3. University of California, 1934.

[10] D. Citrini, *A Contribution to Jet-Pump Design*, vol. 11. Grenoble, France: LaHouille Blanche, 1956.

[11] R. G. Cunningham, "THE JET PUMP AS A LUBRICATION OIL SCAVENGE PUMP FOR AIRCRAFT ENGINES," 1954. [Online]. Available: https://api.semanticscholar.org/CorpusID:137063447

[12] N. H. G. Mueller, "Water Jet Pump," *Journal of the Hydraulics Division*, vol. 90, no. 3, pp. 83–113, May 1964, doi: 10.1061/JYCEAJ.0001059.

[13] R. G. Cunningham, "Gas Compression With the Liquid Jet Pump," *J Fluids Eng*, vol. 96, no. 3, pp. 203–215, Sep. 1974, doi: 10.1115/1.3447143.

[14] R. G. Cunningham and R. J. Dopkin, "Jet Breakup and Mixing Throat Lengths for the Liquid Jet Gas Pump," *J Fluids Eng*, vol. 96, no. 3, pp. 216–226, Sep. 1974, doi: 10.1115/1.3447144.

[15] S. H. Winoto, H. Li, and D. A. Shah, "Efficiency of Jet Pumps," *Journal of Hydraulic Engineering*, vol. 126, no. 2, pp. 150–156, Feb. 2000, doi: 10.1061/(ASCE)0733-9429(2000)126:2(150).

[16] V. Jorge de Oliveira Marum *et al.*, "Performance analysis of a water ejector using Computational Fluid Dynamics (CFD) simulations and mathematical modeling," *Energy*, vol. 220, p. 119779, Apr. 2021, doi: 10.1016/j.energy.2021.119779.

[17] R. Senthil Kumar, S. Kumaraswamy, and A. Mani, "Experimental investigations on a two-phase jet pump used in desalination systems," *Desalination*, vol. 204, no. 1–3, pp. 437–447, Feb. 2007, doi: 10.1016/j.desal.2006.03.546.

[18] A. Shah, I. R. Chughtai, and M. H. Inayat, "Experimental and numerical analysis of steam jet pump," *International Journal of Multiphase Flow*, vol. 37, no. 10, pp. 1305–1314, Dec. 2011, doi: 10.1016/j.ijmultiphaseflow.2011.07.008.

[19] V. Kotak, A. Pathrose, S. Sengupta, S. Gopalkrishnan, and S. Bhattacharya, "Experimental investigation of jet pump performance used for high flow amplification in nuclear applications," *Nuclear Engineering and Technology*, vol. 55, no. 10, pp. 3549–3558, Oct. 2023, doi: 10.1016/j.net.2023.06.017.

[20] A. A. A. Sheha, M. Nasr, M. A. Hosien, and E. Wahba, "Computational and Experimental Study on the Water-Jet Pump Performance," *Journal of Applied Fluid Mechanics*, vol. 11, no. 4, pp. 1013–1020, Jul. 2018, doi: 10.29252/jafm.11.04.28407.

[21] Ankit Rohatgi, “WebPlotDigitizer.” Pacifica, California, Sep. 2022.

[22] K. Aldaş and R. Yapıcı, “Investigation of Effects of Scale and Surface Roughness on Efficiency of Water Jet Pumps Using CFD,” *Engineering Applications of Computational Fluid Mechanics*, vol. 8, no. 1, pp. 14–25, Jan. 2014, doi: 10.1080/19942060.2014.11015494.

[23] C. Wang, L. Wang, X. Wang, and H. Zhao, “Design and numerical investigation of an adaptive nozzle exit position ejector in multi-effect distillation desalination system,” *Energy*, vol. 140, pp. 673–681, Dec. 2017, doi: 10.1016/j.energy.2017.08.104.

[24] H. Wu, Z. Liu, B. Han, and Y. Li, “Numerical investigation of the influences of mixing chamber geometries on steam ejector performance,” *Desalination*, vol. 353, pp. 15–20, Nov. 2014, doi: 10.1016/j.desal.2014.09.002.

[25] K. Hami, “Turbulence Modeling a Review for Different Used Methods,” *International Journal of Heat and Technology*, vol. 39, no. 1, pp. 227–234, Feb. 2021, doi: 10.18280/ijht.390125.

[26] K. Gonçalves Jacinto, S. Varga, and C. Silva, “Strategy to Apply DNS in a Supersonic Ejector,” *U.Porto Journal of Engineering*, vol. 8, no. 2, pp. 1–9, Apr. 2022, doi: 10.24840/2183-6493_008.002_0001.

[27] M. Xu, X. Yang, X. Long, Q. Lyu, and B. Ji, “Numerical investigation of turbulent flow coherent structures in annular jet pumps using the LES method,” *Sci China Technol Sci*, vol. 61, no. 1, pp. 86–97, Jan. 2018, doi: 10.1007/s11431-017-9047-8.

[28] M. Xu, X. Yang, X. Long, and Q. Lü, “Large eddy simulation of turbulent flow structure and characteristics in an annular jet pump,” *Journal of Hydrodynamics*, vol. 29, no. 4, pp. 702–715, Aug. 2017, doi: 10.1016/S1001-6058(16)60782-5.

[29] H. Zi, L. Zhou, and L. Meng, “Prediction and analysis of jet pump cavitation using Large Eddy Simulation,” *J Phys Conf Ser*, vol. 656, no. 1, p. 012142, Dec. 2015, doi: 10.1088/1742-6596/656/1/012142.

[30] “Turbulence models in CFD - RANS, DES, LES and DNS.” Accessed: Jan. 14, 2024. [Online]. Available: https://www.idealsimulations.com/resources/turbulence-models-in-cfd/

[31] H. Xiao and P. Cinnella, “Quantification of model uncertainty in RANS simulations: A review,” *Progress in Aerospace Sciences*, vol. 108, pp. 1–31, 2019, doi: https://doi.org/10.1016/j.paerosci.2018.10.001.

[32] X. L. Yang and X. P. Long, “Numerical investigation on the jet pump performance based on different turbulence models,” *IOP Conf Ser Earth Environ Sci*, vol. 15, no. 5, p. 052019, Nov. 2012, doi: 10.1088/1755-1315/15/5/052019.

[33] L. Asfora, A. dos Santos, and L. de Jesus Nogueira Duarte, “Modeling multiphase jet pumps for gas compression,” *J Pet Sci Eng*, vol. 173, pp. 844–852, Feb. 2019, doi: 10.1016/j.petrol.2018.10.036.

[34] B. D. Landers, “Mixing Characteristics of Turbulent Twin Impinging Axisymmetric Jets at Various Impingement Angles,” 2016. [Online]. Available: http://rave.ohiolink.edu/etdc/view?acc_num=ucin1467987856

[35] S. Rodriguez, *Applied Computational Fluid Dynamics and Turbulence Modeling*. Cham: Springer International Publishing, 2019. doi: 10.1007/978-3-030-28691-0.

[36] S. Rodriguez, *Applied Computational Fluid Dynamics and Turbulence Modeling*. Cham: Springer International Publishing, 2019. doi: 10.1007/978-3-030-28691-0.

[37] F. Moukalled, L. Mangani, and M. Darwish, *The Finite Volume Method in Computational Fluid Dynamics: An Advanced Introduction with OpenFOAM and Matlab*, 1st ed. Springer Publishing Company, Incorporated, 2015.

[38] J. H. Ferziger and M. Perić, *Computational Methods for Fluid Dynamics*, vol. 3. Berlin, Heidelberg: Springer Berlin Heidelberg, 2002. doi: 10.1007/978-3-642-56026-2.

ANNEXES

Annex A. Paper accepted for presentation and publication in the proceedings of ENFHT 2024.

Annex A includes the presentation of the final draft entitled 'Numerical modelling of liquid water jet pumps' Fig. 55 [7], which was accepted with the ID 286 for presentation at ENFHT 2024 - 9th International Conference on Experimental and Numerical Flow and Heat Transfer, held in London, United Kingdom, in April 2024. This paper, authored by Akbar Ravan Ghalati, Manuel Orlando Sandoval Pinto, Sergio Croquer Perez, Sébastien Poncet, Jay Lacey and Hakim Nesreddine, deals with CFD simulations of the internal flow field of jet pumps operating with water. This annex seeks to enrich the contextualization of this research and to support the arguments presented throughout this study.

Proceedings of the 9th World Congress on Momentum, Heat and Mass Transfer (MHMT'24)
London, United kingdom – April 11 – 13, 2024
Paper No. ENFHT XXX (The number assigned by the OpenConf System)
DOI: TBA

Numerical modelling of liquid water jet pumps

Akbar Ravan Ghalati[1], Manuel Orlando Sandoval Pinto[2], Sergio Croquer Perez[3], Sébastien Poncet[3], Jay Lacey[1], Hakim Nesreddine[4]
[1]Civil Engineering Department, University of Sherbrooke
Sherbrooke J1K2R1, Canada
Akbar.Ravan.Ghalati@usherbrooke.ca; Jay.Lacey@usherbrooke.ca
[2]Department of mechanical and aerospace engineering, Universidad de Antioquia
Medellin, Colombia
manuel.sandoval@udea.edu.co
[3]Mechanical Engineering Department, University of Sherbrooke
Sherbrooke J1K2R1, Canada
sergio.croquer.perez@usherbrooke.ca; Sebastien.Poncet@usherbrooke.ca
[4]Laboratoire des technologies de l'énergie, Hydro-Québec, Shawinigan, Canada
nesreddine.hakim@hydroquebec.com

Abstract - This paper focuses on CFD simulations of the internal flow field of jet pumps, which are passive pumping devices. A numerical method based on the RANS equations is proposed, and its abilities are analysed by comparing the obtained results with the available experimental data. The turbulent flow is simulated using Boussinesq hypothesis which relates Reynolds stresses to the mean velocity gradients via turbulent viscosity. The k-ε model (along with the Standard wall function) and the k-ω SST model are used to calculate the turbulent viscosity for solving the flow in near-wall regions. Before checking the validity of the numerical results, Grid Convergence Index (GCI) is estimated to evaluate the mesh. The analysis showed that the maximum GCI is at the cell near the wall with the value of 0.08%. Comparison of the numerical results and experimental data shows that the model captures the jet pump efficiency range with average relative errors of 7.3% and 8.47% for the k-ε and k-ω SST turbulence models, respectively. The numerical results also confirmed that increasing the flow ratio causes the mixing location between the primary and secondary flows to move toward the outlet of the jet pump, which was observed in the previous experimental investigations. The static pressure coefficient, which indicates the pumping effect of the jet pump, is calculated via both of the turbulence models and the comparison with the experimental data showed that the average relative error is 10.68% and 3.21% for the k-ε model and the k-ω SST model, respectively. The study shows that accurate modelling of jet pump parameters is feasible using RANS approach.

Keywords: Jet pump – RANS modelling - GCI analysis – Pumping effect

Fig. 55. Paper accepted for presentation and publication in the proceedings of ENFHT 2024.